Encoding information into spatial modes of light

Bienvenu I. Ndagano
School of Physics
University of the Witwatersrand

A dissertation submitted for the degree of
Master of Science

May 3, 2016

Declaration

By submitting this dissertation electronically, I declare that the entirety of the work contained therein is my own, original work, that I am the sole author thereof (save to the extent explicitly otherwise stated), that reproduction and publication thereof by the University of the Witwatersrand will not infringe any third party rights and that I have not previously in its entirety or in part submitted it for obtaining any qualification.

Bienvenu Irenge Ndagano

Dedication

To my loving parents far away

AND

To the late Amritha Maharaj

Acknowledgements

Throughout this journey, I have had the pleasure to meet and spend time with some wonderful people who have encouraged and supported me. To everyone, I want to say thank you, particularly:

Prof. Andrew Forbes, thank you for taking me under your wing and introducing me to the wonderful world of Optics and Photonics. You have always kept your door open to questions and discussions. I have gained invaluable knowledge about the academic world, how to better myself as a physicist and contribute to the community, in terms of scientific advancement and support to my fellow students.

Dr. Melanie McLaren, you have helped me develop my skills as an experimental physicist. For the long hours you have spent with me in the laboratory and the guidance you have given me with the many things bothering me, I sincerely thank you.

My very first mentors, Dr Angela Dudley and Dr Darryl Naidoo, whom I had the pleasure to meet at the National Laser Centre (NLC) and who have helped me with their guidance both in and out of the laboratory, thank you.

My collaborators whom I had fruitful discussions with and contributed to the work I was able to accomplish, particularly Benjamin Perez-Garcia, Robert Brüning and Abderrahmen Trichili, thank you my friends.

My family and friends who have supported endlessly me throughout the years, I am grateful to you for being such an important part of my life as a person and as a student.

Last but not least, I want to acknowledge the following entities for making this work a reality with their financial support: The Maria-Mater Misericordiae Fondatio

(M-MMF), The University of the Witwatersrand, the National Research Foundation (NRF) and The African Laser Centre (ALC).

Abstract

Spatial modes of light hold the possibility to power the next leap in classical and quantum communications. They provide the ability to pack more information into light, even into single photons themselves, while increasing the level of information security. In this quest, spatial modes carrying orbital angular momentum (OAM) have come under the spotlight due to their discrete infinite dimensional Hilbert space allowing, in theory, for an infinite amount of information to be carried by a photon. Here we study, theoretically and experimentally, spatial modes of two flavours: scalar and vector modes. the dichotomy between the two flavours is in their polarisation characteristics: scalar modes have spatially homogeneous polarisation fields, while vector modes do not. One facet of our work focusses on scalar mode carrying OAM; using digital holographic methods, we demonstrate the techniques used to tailor and analyse scalar optical fields. We discuss principles of generation and detection for scalar modes based on manipulations of the dynamic phase of light with spatial light modulators. We apply these techniques to characterise free-space and optical fibre links, and demonstrate an increase in bandwidth with the additional modal channels. In the other facet of our work, we study vector vortex modes. A particular property exhibited by these modes is the non-separability of their degrees of freedom, a property traditionally associated with entangled quantum states. This raises the question: could quantum entangled systems be modelled with bright sources of vector vortex modes? We answer this question by applying vector vortex modes to the study of quantum transport of entangled states. We borrow techniques from quantum mechanics to evaluate the degree of non-separability of vector vortex modes, using the concurrence as our measure. By determining the evolution of the concurrence, and therefore the entanglement, of vector vortex modes in fibres and free-space turbulent channels, we show that indeed, bright classical sources can be used to model the evolution of entangled quantum states in these channels.

Contents

List of Figures

List of Publications

Peer-reviewed Journal Papers:

1. **Ndagano B.**, Brning R., McLaren M., Duparré M., and Forbes A. (2015), "Fiber propagation of vector modes", *Optics Express*, 23(13), 17330.

2. Brüning B., **Ndagano B.**, McLaren M., Schröter S., Kobelke J., Duparré M., and Forbes A., "Data transmission with twisted light through a free-space to fiber optical communication link", *Journal of optics.* To be published, 2016

International Conferences:

1. Trichili A, Dudley A., Ben Salem A., **Ndagano B.**, Zghal M. and Forbes A., "Encoding information using Laguerre Gaussian modes", *SPIE Proceedings Vol. 9581*, 2015

2. **Ndagano B.**, McLaren M. and Forbes A., "Fiber communication using vector vortex beams", *Photonics West, Optoelectronics and Photonics*, 2016

3. **Ndagano B.**, McLaren M. and Forbes A., "Propagation of vector vortex modes through fibers", *Photonics West, Optoelectronics and Photonics*, 2016

4. **Ndagano B.**, Perez-Garcia B., Mouane O., McLaren M. and Forbes A., "Resilience of vector vortex beams to atmospheric turbulence ", *Photonics West, Optoelectronics and Photonics*, 2016

5. **Ndagano B.**, Perez-Garcia B., Mouane O., McLaren M. and Forbes A., "Propagation of vector vortex beams through turbulence ", *Photonics West, Optoelectronics and Photonics*, 2016

National Conferences:

1. **Ndagano B.**, McLaren M. and Forbes A., "Communication through fibres using cylindrical vector vortex modes", *60th Annual Conference of the South African Institute of Physics*, 2015

2. **Ndagano B.**, Trichili A, Rosales C., Dudley A., Zghal M. and Forbes A., "Encoding information into spatial modes of light", *8th Annual African Laser Centre student workshop*, 2015

3. **Ndagano B.**, Rosales C., Dudley A., McLaren M. and Forbes A., "Twisting light for communication", *7th Annual Cross Faculty Postgraduate Symposium, University of the Witwatersrand*, 2016

Chapter 1

Introduction

Phase, wavelength and polarisation are properties of light upon which current communication networks are based. Previously unexplored, the spatial degree of freedom has been poised as a source for the next leap in classical and quantum communication. Special attention has been given to spatial modes possessing well defined orbital angular momentum (OAM) due to the infinite dimensional Hilbert space that it spans. At the classical level, much effort has been directed towards utilising beams carrying OAM to increase the bandwidth in communication media, namely free-space and optical fibres. A particular type of spatial mode, known as vector vortex modes, possess non-separable degrees of freedom, a property widely associated with entangled quantum states. This raises the possibility of modelling quantum systems with classical light. In this chapter, we motivate our study of spatial modes carrying OAM by first discussing current communication technologies and their limitations. We then expose the concept of OAM, its origin and characteristics, and finally review the concept of entanglement, showing how it arises in spatial modes.

1.1 Motivation

The bulk of the data exchanged worldwide is transported through optical fibres. Current network architectures utilize properties of electromagnetic waves to encode information; these are the phase, polarisation and wavelength. To maximize the fibre capacity, multiplexing schemes have been introduced whereby information is encoded on different channels and simultaneously sent through a single fibre. Time [1], polarisation [2] and wavelength [3] division multiplexing are three of the main schemes used in current networks to take full advantage of the degrees of freedom of light. This is however limited by dispersive effects leading to a spread of the light pulses. Fibre material properties along with manufacturing imperfections lead to group velocity and polarization dispersion [4], thus limiting the amount of information that can be carried by every fibre. At the receiving end of fibre networks, end-users are faced with a speed bottleneck. This is due to the fact that 'fibre to the home' is relatively expensive and in some cases impractical. As such, end-users have to settle for network architectures with reduced capabilities. This is known as the *last mile* problem [5]. To bridge this last mile, cable networks are mostly used, together with free space optical laser links that allow for point-to-point communication [6, 7].

Figure 1.1 shows the impact of scientific and technological advancements in the fibre capacity. Erbium doped fibre amplifier (EDFA) allowed for the amplification of light signals within the fibre, reducing the need for repeaters and extending the range of fibre networks [8]. This was followed by the introduction of wavelength-division multiplexing whereby signals could be sent over multiple wavelengths of light. However, the more information that is sent through a fibre, the lower the signal to noise ratio becomes and the higher the bit error rate. In response to this, forward error correction coding was introduced to allow the fibre to operate closer and closer to its maximum capacity know as the Shannon limit (red dashed line) [9]. More recently, space division multiplexing, has been proposed as a new resource for fibre communication: new fibre designs allow more signals to be transmitted over spatially separated cores inside a single fibre [10]. This technique is, however, still in its early developmental stages and has not yet been implemented on a large scale. With recent research showing that we are approaching the maximum fibre capacity [11] and the ever growing demand in bandwidth, there is therefore a pressing need to improve current fibre networks using additional information channels to sustain the need for high bandwidth long distance communication. For short range communication, bridging the last mile will involve implementing these additional information channels in cost effective schemes that will involve hybrid free-space-fibre optical link.

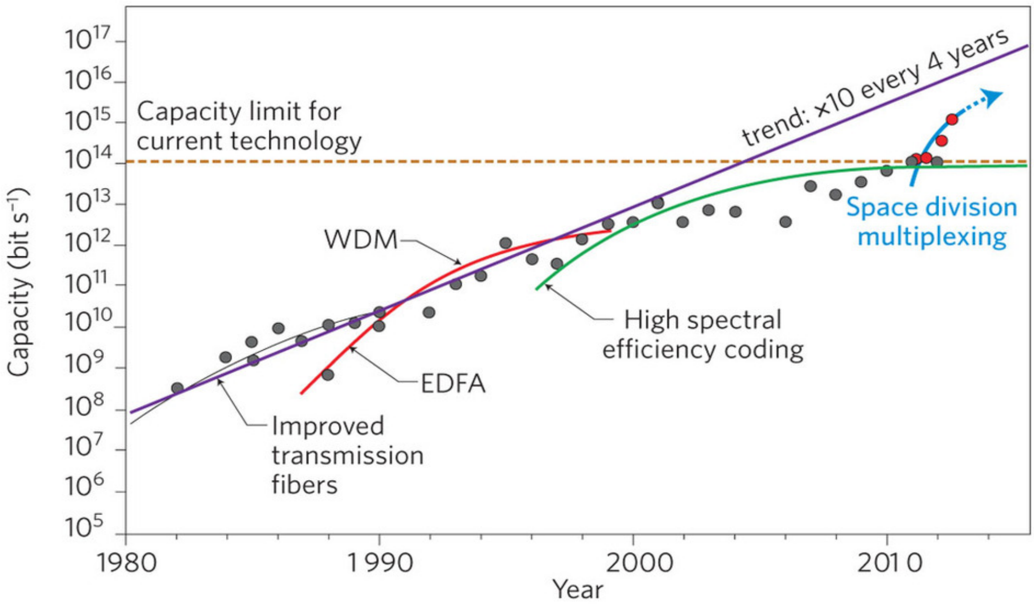

Figure 1.1: Growth of optical fibre capacity over the past 30 years [10].

Over the past two decades, research has been aimed at tapping into a previously unexplored degree of freedom through the spatial modes of light. These spatial modes refer to the transverse profile of the light which is dependent on the medium of propagation. In 1992, Allen *et al.* have shown that some optical laser beams possess well defined orbital angular momentum (OAM) [12]. It was later demonstrated that the OAM of light could be used to encode digital information [13], thereby opening a plethora of potential applications in classical communication. Together with wavelength and polarisation multiplexing, OAM has successfully been implemented to achieve transmission speeds of the order of terabits per second through free space [14] and fibres [15]. In quantum communication, spatial modes have been used to achieve high dimensional entanglement [16–18] which would enhance the security of current quantum key distribution protocols [19] through both free space and fibres.

1.2 Angular momentum of light

The angular momentum of light comes in two flavours: spin angular momentum (SAM) and orbital angular momentum (OAM). The SAM of light, first associated with circular polarization by Poynting in 1909 [20], was experimentally demonstrated by Beth in 1936 when investigating the transfer of angular momentum from a polarised beam to a doubly refracting plate [21]. Beth's results showed that each photon carries $\pm\hbar$ quantum of SAM, corresponding to right or left circular polarisation. The state of polarisation of an electromagnetic wave is given by the plane of oscillation of the electric field as depicted in Fig.1.2(a). A convenient representation of the polarisation states is that proposed by Henri Poincaré in the early 1890s. He proposed a graphical representation of the states of polarisation on the surface of a sphere as shown in Fig.1.2(b). The poles correspond to the polarisations states associated with

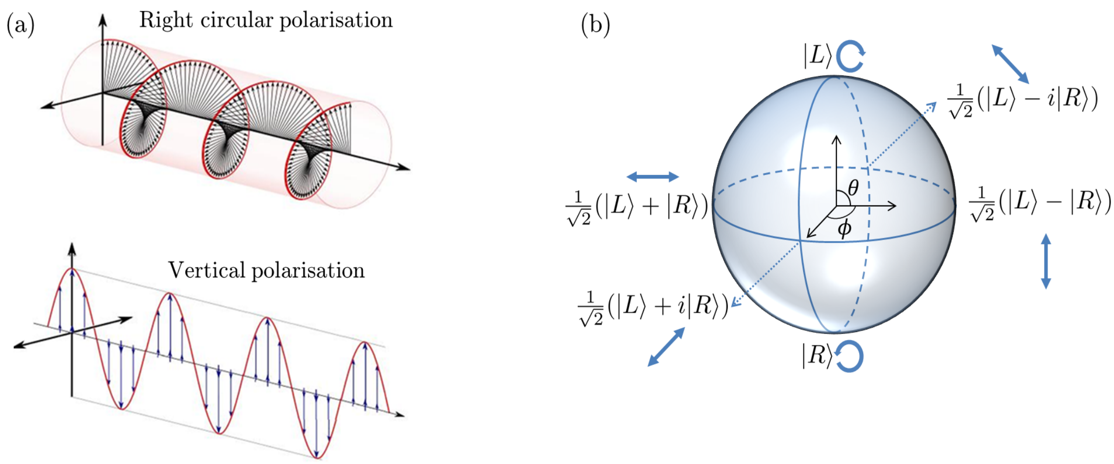

Figure 1.2: Graphical representation of the polarisation states of light. (a) shows the electric field oscillation for circularly and linearly polarised light. (b) Poincaré representation of the states of polarisation

the SAM eigenstates, namely left and right circular polarisation. On the equator are the superposition of these eigenstates with equal weighting for both; these states are the linear polarisation states. In the Poincaré representation, any polarisation state $|\psi\rangle$ can be mapped to a point on the sphere according to the following equation

$$|\psi\rangle = \cos(\theta)|L\rangle + \exp(i\phi)\sin(\theta)|R\rangle \tag{1.1}$$

where θ and ϕ are angles as represented in Fig. 1.2(b) and $|L\rangle$ and $|R\rangle$ are the left and right circular polarisation states respectively. Note that in the above and the rest of this dissertation, we label states (classical and quantum) using Dirac notation.

Long after the demonstration by Beth of the effect of SAM, the orbital component of angular momentum was shown by Allen *et al.* in 1992 to be well defined for laser modes of the Laguerre-Gaussian (LG) type. They showed that in the paraxial limit, that is assuming a slowly varying envelope, laser modes with azimuthal phase dependence of the form $\exp(i\ell\phi)$ possess well defined OAM which can be shown to be quantized as follow: consider an electromagnetic wave propagating in a vacuum and described by the following wave equation

$$\left(\nabla^2 - \frac{1}{c^2}\frac{\partial^2}{\partial t^2}\right) E(\vec{r}, t) = 0, \tag{1.2}$$

where $E(\vec{r}, t)$ is the magnitude of the electric field at position $\vec{r}$ and time t, and c is the speed of light. Assuming a separable solution of the type $E(\vec{r}, t) = U(\vec{r}) \exp[i(kz - \omega t)]$, we arrive at the Helmholtz equation

$$\left(\nabla^2 + k^2\right) R(\vec{r}) = 0, \tag{1.3}$$

where $k \in \mathbb{R}$ and $R(\vec{r}) = U(\vec{r}) \exp(ikz)$ that slowly varies in the transverse plane compared to the longitudinal one (paraxial approximation), Eq. 1.3 becomes

$$\left(\frac{\partial^2}{\partial x^2} + \frac{\partial^2}{\partial y^2} + 2ik\frac{\partial}{\partial z}\right) U(\vec{r}) = 0. \tag{1.4}$$

In the paraxial regime, solutions to Eq. 1.4 in cylindrical coordinates are of the type

$$U(r, \phi, z) = A(r, z) \exp(i\ell\phi). \tag{1.5}$$

The quantization arises by considering the action of the z-component of orbital angular momentum L_z on $U(r, \phi, z)$

$$L_z U(r, \phi) = -i\hbar\frac{\partial}{\partial \phi} U(r, \phi, z) = \hbar\ell U(r, \phi, z). \tag{1.6}$$

Each photon thus carries $\ell\hbar$ quanta of OAM, with $\ell \in \mathbb{Z}$. The state $|\psi\rangle$ of a photon, or any quantum system, can be expressed as a superposition of its eigenstates

$$|\psi\rangle = \sum_i c_i |\psi_i\rangle, \tag{1.7}$$

where the probability amplitude c_i represent the likelihood of the photon being the eigenstate $|\psi_i\rangle$. In terms of communication, this implies that the wider the space of eigenstates is, the more information a photon can carry. thus in a discrete infinite dimensional OAM space, photons can carry an infinite amount of information.

An example of paraxial beams is the set of Laguerre-Gaussian (LG) beams given by

$$U_{p,\ell}(r,\phi,z) = \sqrt{\frac{2p!}{\pi(p+|\ell|)!}}\frac{1}{w(z)}\left(\frac{r\sqrt{2}}{w(z)}\right)^{|\ell|}\exp\left[\frac{-r^2}{w^2(z)}\right]L_p^{|\ell|}\left(\frac{2r^2}{w^2(z)}\right)$$
$$\times\exp\left[\frac{ik_0r^2z}{2(z^2+z_R^2)}\right]\exp\left[-i(2p+|\ell|+1)\arctan\left(\frac{z}{z_R}\right)\right]\exp(i\ell\phi). \quad (1.8)$$

These beams are characterised by a radial index p and an azimuthal index ℓ, the latter representing the OAM eigenvalue. The beam radius, $w(z)$, at a distance z along the propagation axis is given in term of the beam waist $w(0)$ by $w(z) = w(0)\left[(z^2+z_R^2)/z_R^2\right]^{1/2}$ where z_R is the Rayleigh range; it is the distance along the axis of propagation after which the beam doubles in cross-sectional area with respect to the waist and is given by $\pi\omega_0^2/M^2\lambda$, where λ is the wavelength and $M^2 = 2p+\ell+1$ is the beam quality factor which determines deviation of a beam from an ideal Gaussian for which $M^2 = 1$. The set of functions $L_p^{|\ell|}(x)$ are the Laguerre polynomials. The intensity patterns of some LG beams are shown in Fig. 1.3. The radial index p gives rises to concentric rings while the azimuthal index ℓ controls the size of the central vortex.

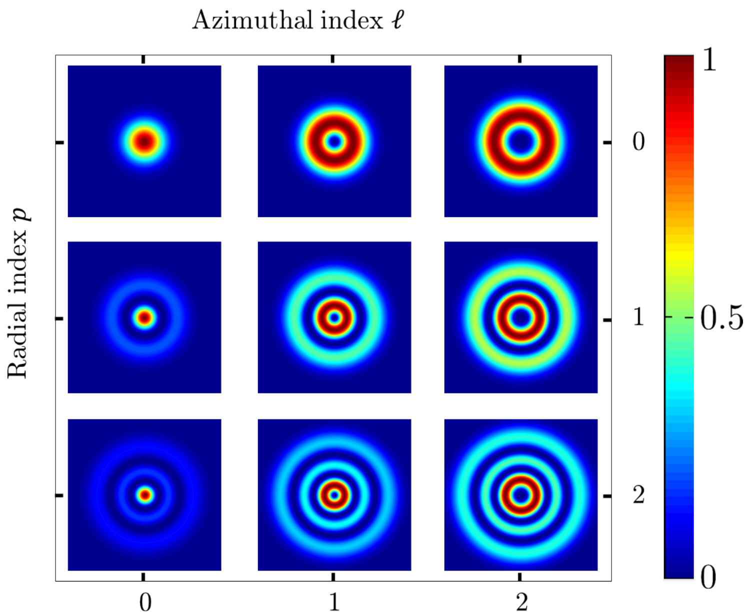

Figure 1.3: Simulated intensity pattern of some Laguerre-Gaussian beams.

Unlike the SAM, the OAM component is not related to polarisation; it is instead associated with the flow of energy of a beam as it propagates. The Poynting vector defines this flow and for an OAM carrying beam, it is helically twisted around the optical axis resulting in a beam having a helical wavefront, as shown in Fig. 1.4 [22]. The azimuthally varying phase possesses a discontinuity on the optical axis of the beam, resulting in the formation of an optical vortex, which manifests in the form of a null intensity along the optical axis.

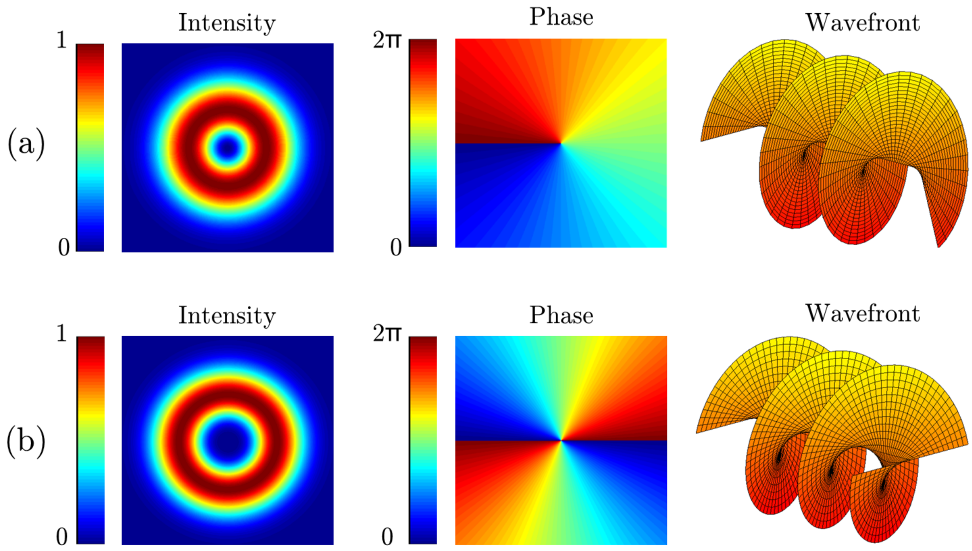

Figure 1.4: Simulated properties of beams carrying OAM of (a) $\ell = 1$ and (b) $\ell = 2$.

As an analogue to the Poincaré representation of SAM, the OAM states in a given subsapce $|\ell|$ can be represented on a unit sphere, a Bloch sphere. The poles represent pure OAM states [23] while those on the equator are superposition modes with equal weighting and varying phase shift. A given state within the subspace $|\ell|$ can be mapped onto the OAM Bloch sphere according to the following equation

$$|\psi\rangle = \cos(\theta)|\ell\rangle + \exp(i\phi)\sin(\theta)|-\ell\rangle. \tag{1.9}$$

Paraxial beams such as the LG beams form a basis set having the following properties

$$\begin{aligned} \langle U_{p,\ell}|U_{k,m}\rangle &\propto \delta_{p,k}\delta_{l,m}, & (1.10)\\ |\Psi\rangle &= \sum_{p=0}^{\infty}\sum_{\ell=0}^{\infty} c_{p,\ell}|U_{p,\ell}\rangle. & (1.11)\end{aligned}$$

Equation 1.10 defines the orthogonality of the modes in the basis: modes with different radial or azimuthal index (OAM) are orthogonal and consequently, they are linearly

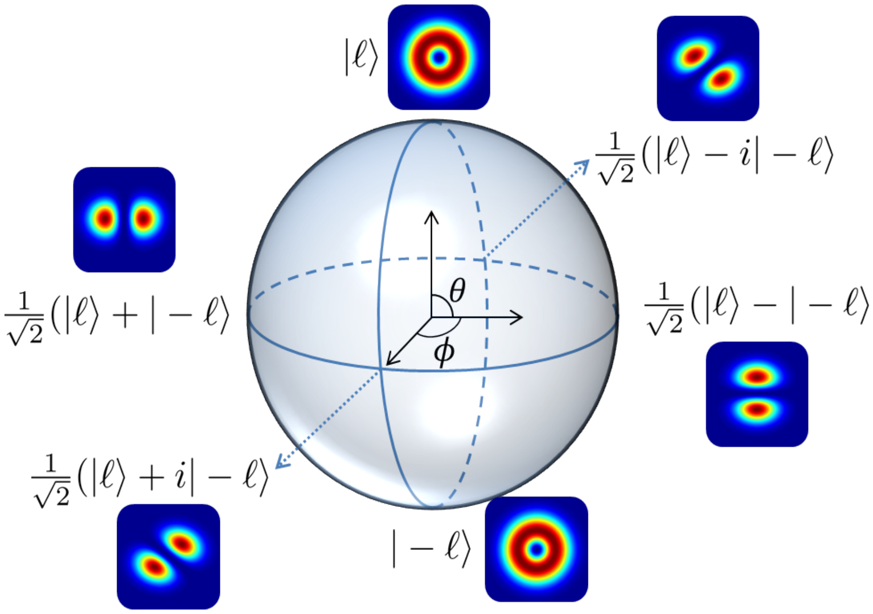

Figure 1.5: Bloch sphere representation of OAM states in a given subspace $|\ell|$

independent. As such, Eq. 1.11 states that an arbitrary optical field $|\Psi\rangle$ can be constructed from a weighted superposition of basis element $|U_{p,\ell}\rangle$, and each of the weighting coefficient can be independently determined.

1.3 Non-separability of entangled states

The concept of entanglement arose in the early years after the birth of quantum mechanics. Quantum entanglement describes the seemingly " spooky action at a distance " - to use Einstein's words - between quantum particles which, at first, appeared to violate the known foundations of special relativity [24]; allowing two systems to exchange information *instantaneously* irrespective of the distance implies superluminal communication, i.e., transfer of information at speeds faster than that of light. In actual fact, information is not exchanged between the entangled systems; rather, knowledge about the state of one of the entangled systems collapses the wavefunction of the other system into a definite state. The concept of entanglement is as follows: consider two *independent* particles A and B in states $|\psi\rangle_A$ and $|\phi\rangle_B$ respectively. The state of the composite system is given by:

$$|\Gamma\rangle_{A,B} = |\psi\rangle_A \otimes |\phi\rangle_B. \tag{1.12}$$

As a consequence of Eq. 1.11, the state $|\Gamma\rangle_{A,B}$ can be expanded in terms of the complete set $\{\psi_n\}$ where ψ_n are the normalized eigenstates of an observable $\mathcal{O}$ of particle A. We then write

$$|\Gamma\rangle_{A,B} = \sum_n |\psi_n\rangle_A \otimes |\phi\rangle_B. \tag{1.13}$$

Any measurement of $\mathcal{O}$ on particle A will result in the collapse its state ψ into one of its eigenstates ψ_n with eigenvalue α_n. A subsequent measurement of an observable $\mathcal{P}$ is performed on particle B. Just as before, we can expand the composite state in terms of the complete set or normalized eigenstates $\{\phi_m\}$ of $\mathcal{P}$. The measurement will therefore collapse the state of the composite system into

$$|\Gamma\rangle_{A,B} = |\psi_n\rangle_A \otimes |\phi_m\rangle_B. \tag{1.14}$$

The above result shows that the state of the composite system is a tensor product state of two local states of particle A and B. More generally, the state of the composite system can be expanded as

$$|\Gamma\rangle_{A,B} = \sum_{n,m} \alpha_{n,m} |\psi_n\rangle_A \otimes |\phi_m\rangle_B, \tag{1.15}$$

with $\alpha_{n,m}$ are positive real coefficients and $\sum\limits_{n,m} \alpha_{n,m}^2 = 1$. This is known as the Schmidt decomposition [25]. Thus, a *separable* composite system is one that can be expressed as a product of the states of its subsystems. In cases where this is not possible, the composite system is said to be *non-separable* or *entangled*. A textbook example of entangled states is that of two fermions in the singlet state

$$|\Gamma\rangle_{A,B} = \frac{1}{\sqrt{2}} \left(|\uparrow\rangle_A |\downarrow\rangle_B - |\downarrow\rangle_A |\uparrow\rangle_B \right), \tag{1.16}$$

where $\{\uparrow, \downarrow\}$ are basis states of spin. Note that here (and the rest of the Dissertation), we omit the tensor product operator for simplicity. A measurement of the spin of fermion A in the above basis determines *with certainty* the state of fermion B and vice versa, regardless of the separation between the fermions - hence the 'spookiness'. This peculiar property of entangled states have been used to demonstrate quantum teleportation [26] and forms the basis of Ekert's quantum key distribution protocol [27].

Analogues to quantum entangled systems have been known to exist at the classical level. Often referred to as classically entangled, these systems are related to a variant quantum entanglement known as hyperentanglement [28]. The entangled state defined by Eq. 1.16 described a composite system of two particles. The ensemble could be viewed as a monolithic system where the two fermions now represent the degrees of freedom as opposed to subsystems. It would be useful to label the degree of freedom differently as follow

$$|\Gamma\rangle = |\alpha_+\rangle|\beta_-\rangle - |\alpha_-\rangle|\beta_+\rangle), \tag{1.17}$$

where $\{\alpha_-, \alpha_+\}$ and $\{\beta_-, \beta_+\}$ are now the bases of the two degree of freedom respectively. We will assume that the basis states are appropriately normalized. This entanglement of degrees of freedom is of particular interest because it can be observed at classical level in the form of spatial modes known as vector vortex modes.

1.4 Non-separable spatial modes

Vector vortex (VV) modes arise as exact solutions of the vector wave equation applied to optical fibres [29].

$$\{\nabla_t^2 + n^2k^2\}\vec{e}_t + \nabla_t\{\vec{e}_t \cdot \nabla_t \left[\ln(n^2)\right]\} = \beta^2\vec{e}_t, \tag{1.18}$$

where n is the refractive index of the fibre, $k = 2\pi/\lambda$ is the wave vector, $\vec{e}_t$ is the transverse electric field and β is the propagation constant of each vector mode solution. The eigensolutions for the higher order vector modes of Eq. 1.18 can be expressed in the form of hyperentangled states as described by Eq.1.17. A particular mode-set of interest in this dissertation is that of the first higher order modes spanning the two dimensional polarisation Hilbert space and the $|\ell| = 1$ OAM subspace. Mathematically, they are given by the following equations

$$|\Psi^\pm\rangle = A(\vec{r})\left(|\ell=-1\rangle|L\rangle \pm |\ell=1\rangle|R\rangle\right), \tag{1.19}$$

$$|\Phi^\pm\rangle = A(\vec{r})\left(|\ell=-1\rangle|R\rangle \pm |\ell=1\rangle|L\rangle\right). \tag{1.20}$$

The radial envelope $A(\vec{r})$ is dependent upon the refractive index profile of the fibre. In terms of fibre modes, the states $|\Psi^+\rangle$, $|\Psi^-\rangle$, $|\Phi^+\rangle$ and $|\Phi^-\rangle$ correspond to the $|\mathrm{TM}_{01}\rangle$, $|\mathrm{TE}_{01}\rangle$, $|\mathrm{HE}_{21}^e\rangle$ and $|\mathrm{HE}_{21}^o\rangle$ modes respectively [29]. These modes are characterized by a null on-axis intensity and an azimuthally varying polarisation map.

The expressions of VV modes given in Eqs. 1.19 and 1.20 are akin to those of a hyperentangled state, given in Eq. 1.17, the 'entanglement' being between the spatial (OAM) and polarisation degrees of freedom. There are however major differences with the entanglement observed at the quantum level, and this classical entanglement. Einstein Podolsky and Rosen (EPR) in their argument on the incompleteness of quantum mechanics [24], defined locality as the fact that a system can only be affected by its immediate surroundings. Under this condition, EPR rejected the idea of quantum entanglement in which particles that are space-like separated would influence each other's states. Light cones in space-time define the past and future of particles; for space-like separated particles, the light cones do not cross unless the particles are allowed to travel faster than light [30].

A common classification of quantum and classical correlation is done with a Bell inequality [31]. The objective of the inequality is to impose boundary on classical correlations which, should only be violated by quantum mechanical counterparts. Consider for example a source emitting in opposite directions two photons A and B, entangled in polarisation, which are then passed through linear polarisers. Let σ^+ and σ^- (χ^+ and χ^-) be orthogonal orientations of the polariser through which photon A (B) is passed. Assuming the polarisation of the two photons are related classically through some hidden variable ξ, Bell defined the correlation between the polarisation states of the photons as

$$E(\sigma, \chi) = \int d\xi \rho(\xi) A(\xi, \sigma) B(\xi, \chi), \tag{1.21}$$

where $\rho(\xi)$ is the probability distribution of the hidden variable ξ. Bell's inequality is summarised by the following statement for classical theories (hidden variable theory)

$$|S| = E(\sigma^+, \chi^+) - E(\sigma^+, \chi^-) + E(\sigma^-, \chi^+) + E(\sigma^-, \chi^-) \leq 2. \tag{1.22}$$

Thus, if $|S| > 2$, entanglement would be a feature of quantum mechanics, devoid of any hidden variable, and this has been proved; violations of Bell's inequality and locality as defined above has been shown for entangled systems [32]. Interestingly, vector vortex beams have also been shown to violate Bell's inequality [33, 34] but not locality as defined by EPR. There is therefore a need to emphasise that although classical systems may exhibit a form of entanglement, they cannot be treated as quantum objects.

The non-separability of vector vortex modes can be illustrated by observing the effect of a measurement on one of the DoFs. Figure 1.6 shows how polarisation measurements collapse the spatial DoF into particular states on the OAM Bloch sphere. Conversely, for a particular VV mode, a measured state on the OAM Bloch sphere can be mapped to a particular state on the Poincaré sphere.

As VV modes are formed from an incoherent superpositions of hybrid OAM-polarisation basis states, one would wonder whether VV modes can be mapped to points on a sphere as were the OAM and polarisation states. This is indeed possible as

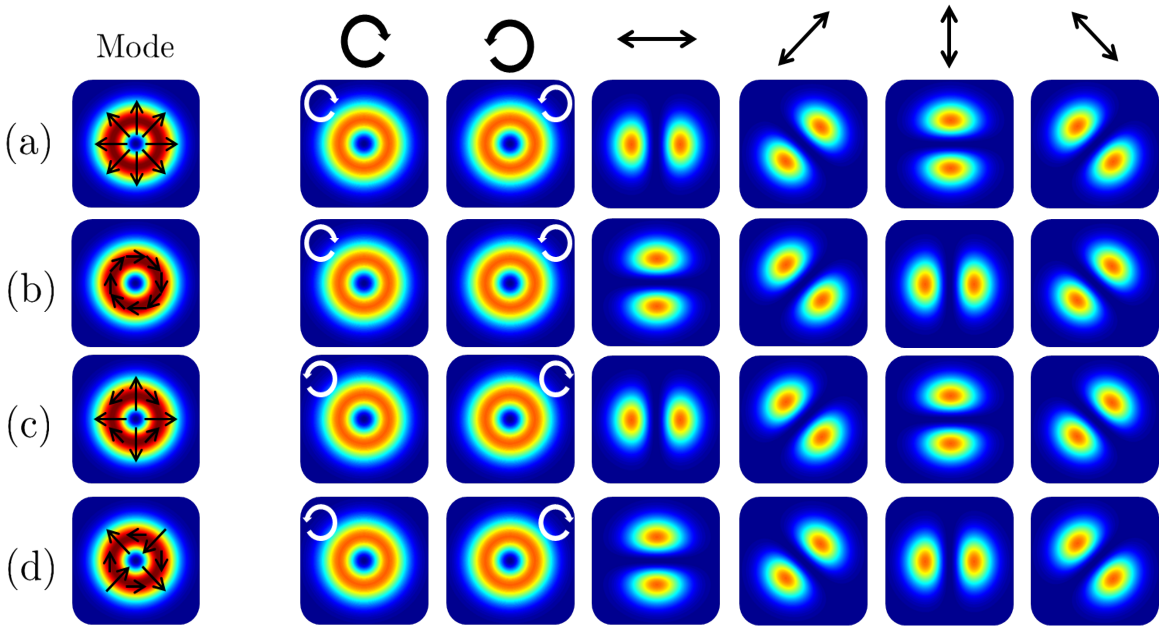

Figure 1.6: Mode fields of the first four higher order vector vortex beams. The black arrow represent the polarisation measurements performed on a (a) $|\mathrm{TM}_{01}\rangle$, (b) $|\mathrm{TE}_{01}\rangle$, (c) $|\mathrm{HE}_{21}^{e}\rangle$ and (d) $|\mathrm{HE}_{21}^{o}\rangle$ mode. The white arrows show the OAM handedness.

shown in Fig. 1.7. Vector vortex modes of the $|\Psi\rangle^{\pm}$ and $|\Phi^{\pm}\rangle$ types can be mapped to points on a sphere known as a higher order Poincaré sphere (HOPS) [35]. The poles correspond to basis OAM-polarisation states while the vector vortex beams are located on the equator of the HOPS.

Vector vortex beam have the potential to classically emulate qubits in classical processes analogous to those encountered in the quantum world [36–38]. As such, they allow to answer some questions about quantum systems by probing a classical analogue. In this dissertation, we will focus on the use of qubits (quantum bits) for communication. More specifically, one question will be at the centre of our study: How are (entangled) qubits affected by communication channels? We will approach this question by studying the behaviour of VV beams in various communication channels.

1.5 Outline

Our work flow is as follows: In Chapter 2 we will demonstrate techniques to generate and detect scalar beams with digital holographic techniques and vector vortex beams using custom designed inhomogeneous anisotropic phase plates. We have shown that vector vortex modes are mathematically entangled. In quantum mechanics, a well-known method to quantify entanglement is through the concurrence. We will demon-

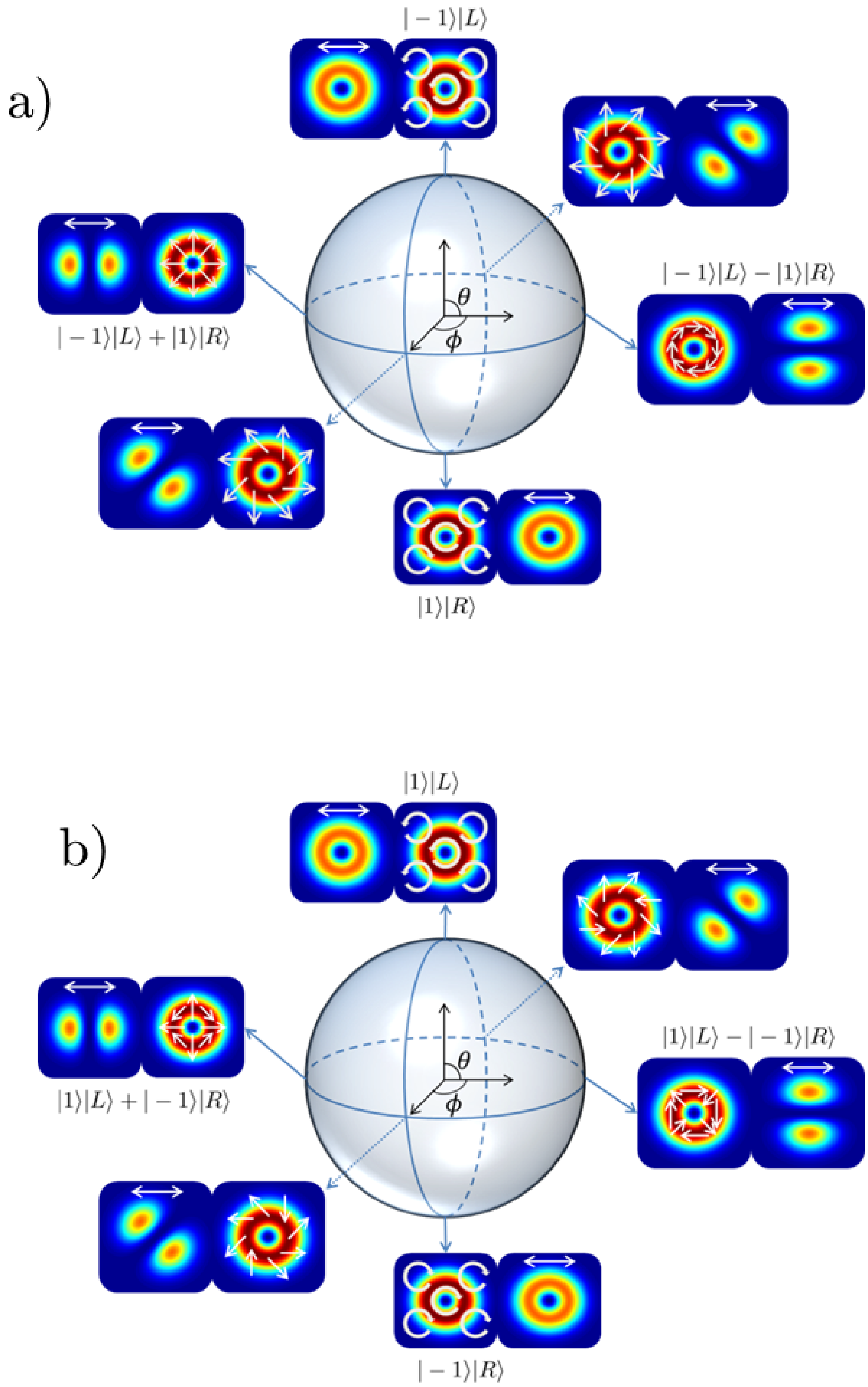

Figure 1.7: Higher order Poincaré sphere for a) the $|\Psi^{\pm}\rangle$ and b) the $|\Phi^{\pm}\rangle$ vector vortex modes.

strate techniques to evaluate the concurrence of vector vortex mode by performing a full state tomography.

In Chapter 3 we will apply the techniques demonstrated in the previous chapter to characterize communication channels for long distance data transfer. Two channels will be of interest: free-space and optical fibres. In free space, we will demonstrate the mechanisms leading to decoherence of entangled qubits through atmospheric turbulence. In fibres, we will show entanglement preservation during propagation.

In Chapter 4 we will demonstrate, using both scalar and vector modes, data transfer on two real-world simulated optical links. On one hand, we will employ single bit encoding techniques to transfer data on scalar beams in a last-mile free-space-fibre link. On the other hand, we will demonstrate multi-bit encoding with multiplexed vector vortex beams in a simulated long distance, weak turbulence, propagation.

Finally we conclude by highlighting the impact of our work in the quest to increase data transmission speeds using spatial modes of light.

Chapter 2

Experimental techniques

Here we present the techniques used to tailor optical fields through manipulation of the dynamic and geometric phase of light. In particular we explore optical fields that possess well defined OAM. Firstly, we look at optical modes in which the amplitude and polarisation components can be treated independently of each other. We will label these modes as *scalar modes*. We demonstrate active and passive methods to generate and analyse their OAM content through manipulation of the dynamic phase of light. Secondly, we focus on a more exotic type of optical fields in which the amplitude and polarisation components are not separable; that is they cannot be treated independently of each other. We will label these modes as *vector modes*. We will narrow our interest to vector modes that exhibit azimuthal symmetry in polarisation and amplitude and carry OAM; these are called vector vortex modes. We will demonstrate techniques to generate and detect these modes that employ the geometric phase of light. Finally, we will demonstrate a characterisation technique based on quantum mechanics to discern between modes of the scalar and vector flavours.

2.1 Generation and detection of scalar modes

With the demonstration by Allen *et al.* that some optical fields possess well defined orbital angular momentum (OAM) [12], various methods have been devised to generate OAM carrying beams. The early methods were aimed at manipulating the *dynamic* phase of a Gaussian laser beam. The term dynamic refers to the phase a beam acquires as a result of its propagation through a particular medium. Early attempts to generate OAM carrying beams involved the use of spiral phase plates [40]. The technique spatially modulates the phase of a laser beam by passing it through a optical element with constant refractive index but azimuthally varying thickness. The result is a beam having azimuthally varying phase. Mathematically this phase modulation is described as follows: consider a beam with flat wavefronts normally incident on a spiral phase plate. The azimuthally varying thickness creates a pitch α between sections of the plate as shown in Fig. 2.1. When passing through the plate, the rays are refracted at an angle θ upon exiting the plate. The phase shift δ_d incurred as a result of the propagation through the phase plate is given by:

$$\delta_d = \vec{k} \cdot \vec{r} = \frac{2\pi}{\lambda} \left(n_p - n_0\right) d(x, y), \tag{2.1}$$

where $\vec{k}$ is the wave-vector, $\vec{r}$ is the optical path, λ is the wavelength, n_p and n_0 are, respectively, the refractive indices of the phase plate and air. the refractive index of air is taken to be that of the vacuum ($n_0 = 1$). For the output beam to carry an

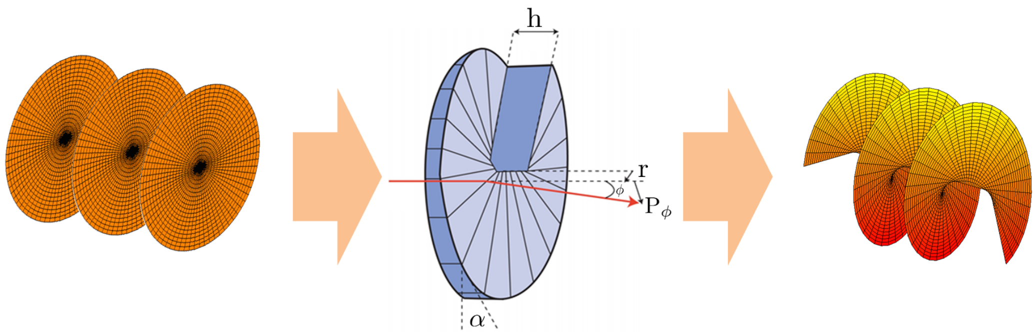

Figure 2.1: OAM phase modulation using a spiral phase plate. The phase plate causes an azimuthally varying phase which results in a beam having a helically twisted wavefront.

OAM charge of ℓ, we require $\delta_d = \ell\phi$, where ϕ is the azimuthal field distribution of the beam. Thus one obtains the expression of the local thickness of the plate as:

$$d(x, y) = \frac{\ell\lambda}{2\pi(n-1)}, \tag{2.2}$$

where $n = n_p$. The dependence of the thickness on the wavelength has made spiral phase plates very difficult to manufacture for optical wavelengths as the size h of the steps needs to be comparable to the wavelength [39, 41]. The angular momentum imparted on the incident beam can be obtained by considering the angular deviation resulting from the refraction of the rays exiting the phase plate. A distance r from the centre of the plate, the angle of incidence obeys the following relation:

$$\sin(\theta_1) \approx \theta_1 = d/r = \frac{\ell\lambda}{2\pi(n-1)r}. \tag{2.3}$$

Note that the above approximation can be made as we are in the paraxial regime. Due to the geometry of the phase plate, the ray exiting will not be refracted in the same plane as the incident ray. Such a ray is said to be skewed and Snell's law relating the two angles is $\phi = (n-1)\theta_1$ [42]. Thus we obtain the following expression for the angular deviation at the output of the phase plate:

$$\phi = \frac{\ell\lambda(n-1)}{2\pi(n-1)r} = \frac{\ell\lambda}{2\pi r} = \frac{\ell}{k_0 r}. \tag{2.4}$$

Each photon in the incident ray has linear momentum $P = \hbar k_0$, with $k_0 = 2\pi/\lambda$. In the paraxial regime, one finds that the linear momentum transferred in the $\hat{\phi}$ direction, P_ϕ, is given by

$$P_\phi = P\frac{\partial P}{\partial \phi} = P\phi = \frac{\ell\hbar}{r}, \tag{2.5}$$

with associated angular momentum

$$L_z = \vec{r} \times \vec{P_\phi} = \hbar\ell. \tag{2.6}$$

Spiral phase plates can therefore be designed to impart $\hbar\ell$ quantum of OAM to photons. In addition to the technical challenges in manufacturing, spiral phase plates need to be custom made to produce a particular OAM carrying beam at a specific wavelength. This created the need for more versatile techniques to generate OAM beams. Current state of the art techniques address this need using digital holography. Figure 2.2 illustrate how the hologram of a spiral phase plate is generated by interfering an OAM carrying beam with a plane wave. Digital holographic techniques directly modulate the phase of light using computer generated holograms. This is achieved by imposing a linear phase on the optical phase pattern, the sum modulo 2π [22]. This digital modulation allows for complex patterns of light to be generated on-demand with a few clicks on a computer. This technique has shown application

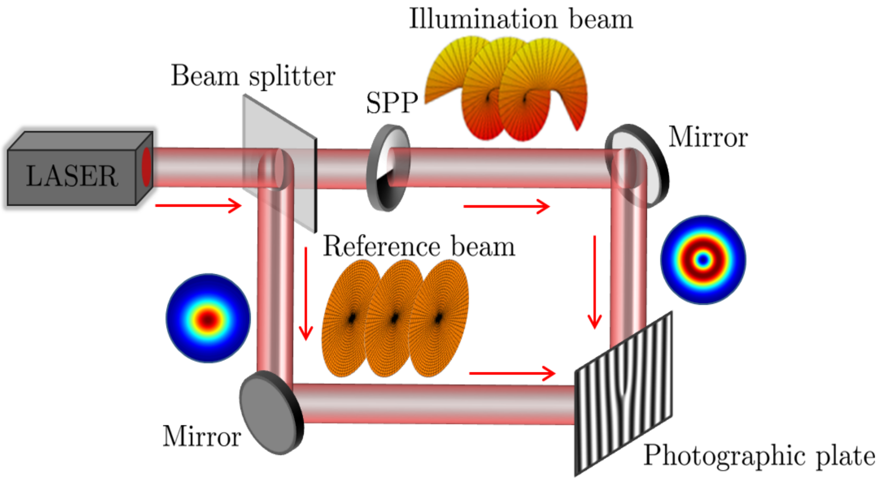

Figure 2.2: Holographic generation of OAM phase screens. A spiral phase plate (SPP) imparts OAM onto a Gaussian beam, which is interfered with reference beam having planar wavefronts, to produce a 'forked' hologram.

in other fields such as optical trapping and tweezing [43, 44], pulse shaping [45], microscopy [46, 47], or three dimensional cell imaging [48] just to name a few.

When it comes to dynamically modulating the phase of light, a device of choice currently used is a spatial light modulator (SLM). It is a pixelated liquid crystal display that is electronically controlled, with each of the pixels individually addressed. By applying an electric field $\vec{E}$ across a pixel, the orientation of the crystals can be fine-tuned. This results in a change of refractive index which is proportional to the voltage applied across the pixel. The phase shift induced is related to the applied voltage as follows:

$$\delta_d \propto l\frac{2\pi}{\lambda}V \tag{2.7}$$

where l is the length of each pixel and V is the voltage applied. The SLM used in the work presented throughout this dissertation is a phase-only HOLOEYE with a 1920×1080 pixel resolution, a pixel width of 8 μm and a 50 Hz refresh rate. Phase-only refers to the ability of the SLM to only modulate in phase, not amplitude. This raises an important question: how can one generate optical fields with azimuthal and radial dependence such as LG beams? This is achieved through complex amplitude modulation, a technique developed by Arrizón *et al.*[49]. The principle of the encoding is as follows: consider an optical field given by

$$U(x, y) = A(x, y)\exp(i\phi(x, y)), \tag{2.8}$$

where $A(x,y)$ and $\phi(x,y)$ are real value functions representing, respectively, the amplitude and phase of the optical field. The phase-only SLM can be modelled by a transmission function

$$T(x,y) = \exp(iS(x,y)), \tag{2.9}$$

where $S(x,y)$ is the phase modulation of the hologram on display. The above expression has no amplitude term that can be manipulated. To modulate both the phase and amplitude to produce the field $U(x,y)$, the SLM must be 'taught' to do so. Arrizón *et al.* showed that the modulation suited for liquid crystal SLMs to produce a field $U(x,y)$ given in Eq. 2.8 is of the form

$$S(x,y) = f(A(x,y))\sin(\phi(x,y)), \tag{2.10}$$

where $f(A(x,y))$ is a function of the amplitude and is specific to the radial envelope of the optical field $A(x,y)$, obtained by inverting the first term in the Fourier expansion of $S(x,y)$ in the domain of ϕ. This makes it possible to encoded a large variety of optical fields in both amplitude and phase using a phase-only SLM.

In addition to their encoding functionality, SLMs can also be used as a decoder for OAM carrying beams. The simplest detection system one could imagine is a scheme in which the generation process is reversed. Probing the OAM content of a beam would however require one to probe all the possible OAM eigenstates. This again shows the advantage of digital holography over static detection systems that would involve spiral phase plates or holographic plates. The method we will present can be applied to the reconstruction of an arbitrary optical field. The method is as follow: an arbitrary optical field $U(x,y)$ can always be expanded in terms of a complete set of basis functions $\psi(x,y)$ as follows:

$$U(x,y) = \sum_i c_i \psi_i(x,y), \tag{2.11}$$

$$c_i = \int dA\ \psi_i^*(x,y)U(x,y). \tag{2.12}$$

Though not unique, our basis of choice will be the Laguerre-Gaussian basis expressed in Eq. 1.8. The LG basis is orthonormal and complete; as such, the coefficients c_i in the field expansion can be independently determined. Experimentally, this can be digitally achieved using a SLM. By directing the optical field $U(x,y)$ incident on the SLM where holograms of functions ψ_i^* have been encoded, the first order diffracted beam will be expressed as:

$$F(x,y) = \psi_i^*(x,y)U(x,y). \tag{2.13}$$

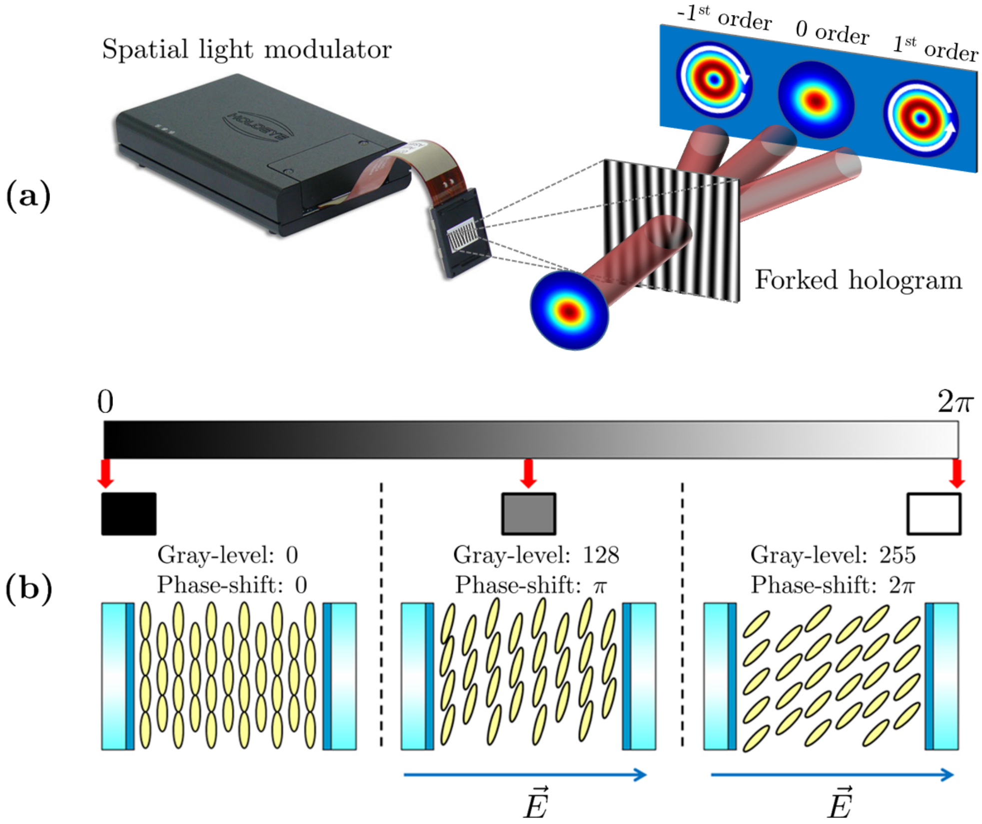

Figure 2.3: Phase modulation using a spatial light modulator. **(a)** shows a Gaussian beam modulated by a forked hologram encoded on a SLM. The 1^{st} order diffracted beam carry the phase modulation. **(b)** The SLM modulation is achieved by modulating the gray-level of each pixel, with each level corresponding to a particular phase shift.

To perform the inner product in Eq. 2.12, we first Fourier transform Eq. 2.13 to obtain:

$$\mathcal{F}\{F(x,y)\} = F(k_x,k_y) = \iint dA\ \psi_i^*(x,y)U(x,y)\exp[i(k_x x + k_y y)] \tag{2.14}$$

Setting $k_x = k_y = 0$, which is equivalent to being on the optical axis in the Fourier plane, one obtains Eq. 2.12. Experimentally, one only has access to the field intensity. We therefore define the state coefficients as:

$$|c_i|^2 = |F(0,0)|^2 = \left|\iint dA\ \psi_i^*(x,y)U(x,y)\right|^2 = |\langle\psi_i|U\rangle|^2. \tag{2.15}$$

Given that each of the states $\psi_i(x,y)$ define optical modes (vortex modes in this instance), this method is referred to as modal decomposition; an optical field is decomposed into a superposition of orthogonal basis modes [50–52]. Figure 2.5**(a)** shows

(a)

(b)

(c)

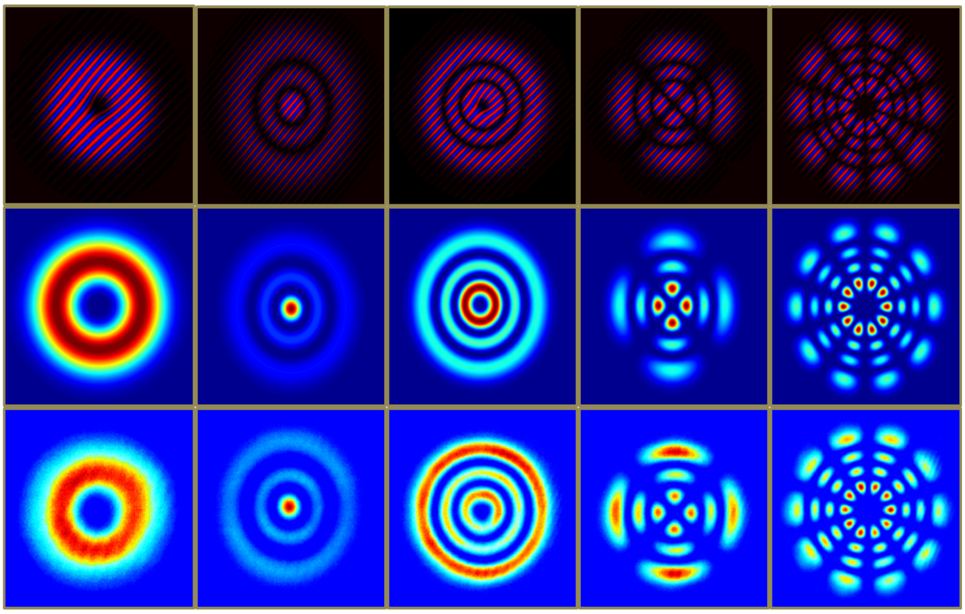

Figure 2.4: Experimental generation of LG beams. **(a)** shows the encoded holograms, **(b)** the simulated mode intensity and **(c)** the experimentally measured mode intensities.

the experimental setup used to perform the modal decomposition of vortex beams. Light from a laser was modulated using SLM-1. The forked (no radial dependence) holograms encoded created a diffraction pattern, of which the first order was selected using a physical aperture. Successive forked holograms were subsequently encoded on SLM-2 with radial index $p = 0$ and OAM charge ranging from $\ell = -5$ to $\ell = 5$. The Fourier lens, placed one focal length away from SLM-2, performed transformed the output as per Eq. 2.14 and the on-axis intensity was measured at the Fourier plane as per Eq. 2.15. For the generated vortex beams, the output of the modal decomposition is given by:

$$|\langle\psi_i|U\rangle|^2 = \left|\iint dA\ \tilde{A}^*(x,y)A(x,y)\exp(i(\ell-\ell')\phi)\right|^2 \tag{2.16}$$

$$|\langle\psi_i|U\rangle|^2 = \left|\tilde{A}^*(x,y)A(x,y)\right|^2 \delta_{\ell',\ell}. \tag{2.17}$$

From the above, one would measure a non-zero on-axis intensity, if and only if, the two holograms on both SLMs have identical topological charge as illustrated in Fig. 2.5**(b)**.

Expressing a beam as a weighted superposition of orthogonal modes of a particular basis set is an extremely powerful technique. Particularly in the field of optical communication using spatial modes. In addition to be effective in decoding information carried by optical modes, it provides the ability to study perturbative media. In

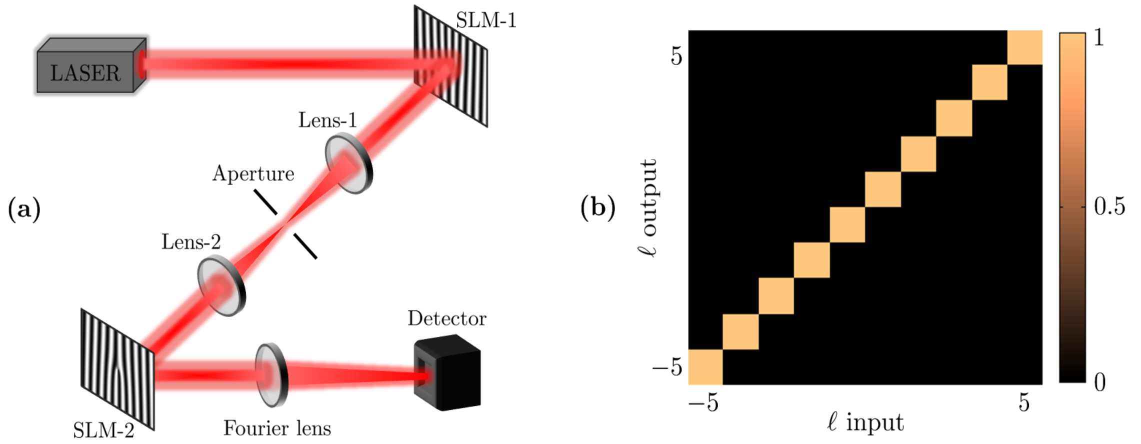

Figure 2.5: Experimental generation and detection of OAM carrying beams. **(a)** shows the experimental where a laser beam from a laser is modulated on SLM-1 with a forked hologram. The modal decomposition is carried out using SLM-2 and the Fourier lens and the intensity is measured on the detector. **(b)** shows the modal decomposition of vortex modes with topological $\ell = -5$ to $\ell = 5$ excluding $\ell = 0$.

the next Chapters, we will apply these techniques to study two media of choice in communication: optical fibres and free space.

2.2 Generation and detection of vector vortex modes

Vector vortex (VV) modes, unlike their scalar counterpart, have spatially inhomogeneous field distributions. That is, the spatial distribution depends on the observer making the measurement: for example, different observers making different polarisation measurements will observe different field distributions. A convenient geometric way of looking at the relation between the polarisation and the spatial distribution is using the Poincaré sphere. For scalar modes, all the points across the beam profile can be mapped to a single point on the Poincaré sphere. In the case vector beams, this is not the case. As such, generating a VV beam requires optical elements that can modulate the phase **and** the polarisation at every point across the beam profile.

Over the years, various methods have been proposed to generate VV beams, some classified as passive and others as active [53]. The active generation of VV beam is generally achieved inside a laser cavity where devices are introduced to force the laser to oscillate in a particular VV mode[53]. To this end, two phenomena come into play to create the inhomogeneous spatial fields of VV beams: birefringence and dichroism. Materials in which the refractive index is dependent upon the polarisation are called birefringent while those in which the absorption is dependent upon the polarisation are called dichroic. In the earliest active methods used to generate VV beams, both birefringence [54] and dichroism [55] have been used as polarisation mode selectors.

Some passive methods also use birefringence and dichroism into mode analyser to generate a particular type of VV beam. An optical element with transmission axes matching the polarisation map of a VV beam is made of birefringent or dichroic material to locally select polarisation components [56]. Another method based on spatially variant phase retarders utilizes a similar concept but instead the optical element generating VV beam locally rotates polarisation [57]. More exotic methods involve the use of spatial light modulators [58] and stressed fibre lasers [59].

The method we present in this work to generate VV beam is a passive method that utilises a an optical element with spatially variant birefringence known as a q-plate [60]. The locally varying birefringence causes the components of polarisation to experience different phase retardations. The dynamic phase incurred as a result of the propagation through such a birefringent material is given by

$$\delta_d = \left(\frac{n_e + n_o}{2}\right)\frac{2\pi}{\lambda}d(x,y), \tag{2.18}$$

where n_o and n_e are the 'ordinary' and 'extraordinary' rays respectively. These rays are defined with respect to what is referred to as the optic axis. The varying birefringence makes a material anisotropic; the properties of the material vary with the axis of propagation of a ray. In some materials, the anisotropy is directional. This direction is what is known as the optic axis. The terms 'ordinary' and 'extraordinary' refer to rays perpendicular and parallel to the optic axis, respectively [61]. In addition to this dynamic phase, the varying birefringence gives rise to a second type of phase that can mathematically be demonstrated with ease. Similarly to wave-plates polarisers in the Jones formalism, a q-plate can be represented by the following square matrix

$$T(q) = \begin{pmatrix} \cos(2q\phi) & \sin(2q\phi) \\ \sin(2q\phi) & -\cos(2q\phi) \end{pmatrix}, \tag{2.19}$$

where q is the topological charge of the plate and ϕ is the azimuthal field distribution.

Now consider a left circularly polarised beam propagating though the q-plate . Its polarisation state can be expressed as:

$$|L\rangle = \frac{1}{\sqrt{2}}(|H\rangle + i\,|V\rangle) = \frac{1}{\sqrt{2}}\left[\begin{pmatrix}1\\0\end{pmatrix} + i\begin{pmatrix}0\\1\end{pmatrix}\right], \tag{2.20}$$

where $|H\rangle$ and $|V\rangle$ are the horizontal and vertical polarisation states, respectively. After passing through the q-plate , the electric field will be given by

$$\vec{E}_{out} = \frac{1}{\sqrt{2}} \begin{pmatrix} \cos(2q\phi) + i\sin(2q\phi) \\ \sin(2q\phi) - i\cos(2q\phi) \end{pmatrix} = \frac{1}{\sqrt{2}} e^{2iq\phi} |R\rangle. \tag{2.21}$$

As a result of the anisotropy, the horizontal and vertical components gain a phase $\exp(2iq\phi)$. This phase, unlike the dynamic one, does not depend on the optical path length, but rather on the geometry (spatial variance) of anisotropy [62]. Hence, this phase has been labelled as the *geometric* phase or the Berry phase after Sir Michael Berry who rediscovered it in 1984 [63] based on the analysis of state of polarisation of interfering plane waves from Pancharatnam in 1956 [64]. A graphical way to explain the geometric phase is by considering the precession of a pendulum on a sphere [65] as shown in Fig. 2.6. The pendulum is taken from the pole at 1, along a line of longitude to the equator at 2, then along the equator to 3 before returning to 1. The dynamic phase incurred as a result of the evolution of the pendulum is given by a path integral over a close line that is zero. Thus, the pendulum acquires no dynamic phase. Figure 2.6 shows however that the final state $|\psi\rangle_f$ of the pendulum is given by

$$|\psi\rangle_f = \exp(i\Phi)|\psi\rangle_1. \tag{2.22}$$

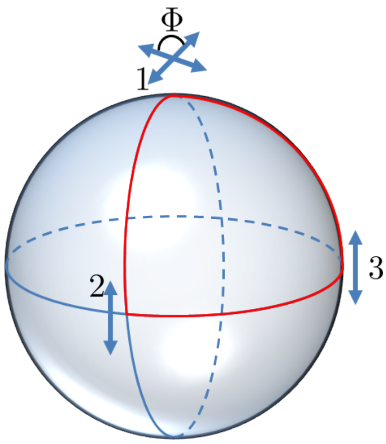

Figure 2.6: Precession of the Focault pendulum on a sphere. The state of the pendulum is evolved in the sequence $1 \to 2 \to 3 \to 1$. Upon returning to its original state, the pendulum acquires a geomtric phase Φ

In 1984, Berry showed that the phase factor Φ is related to the solid angle subtended by the closed path. The total phase δ_t acquired by a beam upon propagation through an anisotropic medium is therefore given by

$$\delta_t = \left(\frac{n_e + n_o}{2}\right) \frac{2\pi}{\lambda} d(x, y) \pm \delta_g, \tag{2.23}$$

where δ_g is the geometric phase. The $\pm$ sign is due the left and right circular polarisations experiencing geometric phases of opposite signs.
At this point, it is worth noting that the geometric phase from Eq. 2.21 is associated with the azimuthal field distribution ϕ, as is the OAM. As such, q-plates are manufactured to generate beams of photons having quantized OAM according to the following transformation rules:

$$|\ell\rangle|L\rangle \xrightarrow{q\text{-}\mathbf{plate}} |\ell+2q\rangle|R\rangle \tag{2.24}$$
$$|\ell\rangle|R\rangle \xrightarrow{q\text{-}\mathbf{plate}} |\ell-2q\rangle|L\rangle. \tag{2.25}$$

The four VV modes of interest in this dissertation were generated using q-plates as shown in Fig. 2.7. Linearly polarised Gaussian beams were transformed with q-plates with topological charges $q = \pm 1/2$. The transformations are as follows:

$$|0\rangle|H\rangle = \frac{1}{\sqrt{2}}\left(|0\rangle|L\rangle + |0\rangle|R\rangle\right) \xrightarrow{q_{1/2}} \frac{1}{\sqrt{2}}\left(|1\rangle|R\rangle + |-1\rangle|L\rangle\right) \tag{2.26}$$
$$|0\rangle|V\rangle = \frac{1}{i\sqrt{2}}\left(|0\rangle|L\rangle - |0\rangle|R\rangle\right) \xrightarrow{q_{1/2}} \frac{1}{i\sqrt{2}}\left(|1\rangle|R\rangle - |-1\rangle|L\rangle\right) \tag{2.27}$$
$$|0\rangle|H\rangle = \frac{1}{\sqrt{2}}\left(|0\rangle|L\rangle + |0\rangle|R\rangle\right) \xrightarrow{q_{-1/2}} \frac{1}{\sqrt{2}}\left(|-1\rangle|R\rangle + |1\rangle|L\rangle\right) \tag{2.28}$$
$$|0\rangle|V\rangle = \frac{1}{i\sqrt{2}}\left(|0\rangle|L\rangle - |0\rangle|R\rangle\right) \xrightarrow{q_{-1/2}} \frac{1}{i\sqrt{2}}\left(|-1\rangle|R\rangle - |1\rangle|L\rangle\right). \tag{2.29}$$

By observing the intensity patterns of the different VV beams after a polariser, we confirmed the non-separability of the polarisation and OAM degrees of freedom. Just as we showed in the case of scalar beam, the encoder (q-plate) can also be used in reverse as a decoder. The detection method we use for VV beams follows the same principle as that of the scalar modal decomposition: we perform inner product measurements of an optical field with orthogonal basis states. The only difference is that, the basis states are VV modes. The method is as follows: consider an arbitrary optical field $|\Psi\rangle$ that can can be either scalar or vectorial in nature. We pass this optical field through a q-plate and project it onto one of the linear polarisation basis states. This is effectively reversing the generation method depicted in Fig. 2.7. Mathematically, we will represent the above steps by the following equation

$$I = \langle\sigma|T(q)|\Psi\rangle, \tag{2.30}$$

where $\langle\sigma|$ represents the projection onto a linear polarisation basis state, say horizontal or vertical for example. The transmission matrix $T(q)$ is Hermitian; that is $T(q) = T^{\dagger}(q)$. As such, we can write

$$I = \langle\sigma|T^{\dagger}(q)|\Psi\rangle = \langle\Gamma|\Psi\rangle, \tag{2.31}$$

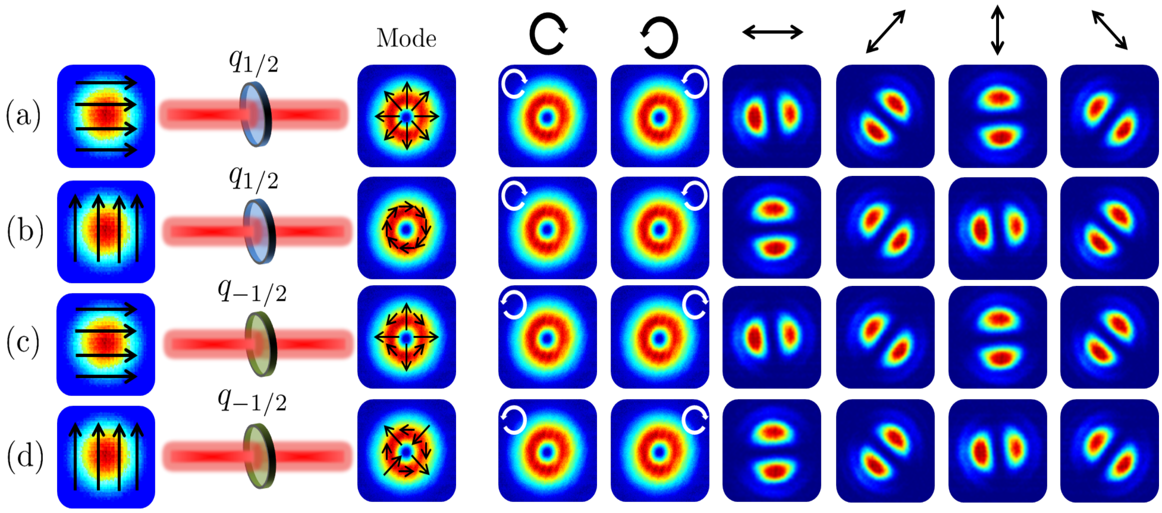

Figure 2.7: Experimental generation of the first four higher order vector vortex beams. Linearly polarised Gaussian beams with $\ell = 0$ OAM are passed through q-plates with topological charge $q = \pm 1/2$. The generated **(a)** $|\text{TM}_{01}\rangle$, **(b)** $|\text{TE}_{01}\rangle$, **(c)** $|\text{HE}^{e}_{21}\rangle$ and **(d)** $|\text{HE}^{o}_{21}\rangle$ beams are then observed through a linear polariser. The black arrows show the polarisation and the white arrows the OAM handedness.

where $|\Gamma\rangle$ is a vector vortex mode according to the the transformation rules of a q-plate . We are thus effectively projecting our arbitrary optical field $|\Psi\rangle$ onto VV basis states. To obtain an expression for the spatial distribution of the output optical field $F(x, y)$, we first introduce the projection operator for a two-dimensional position space:

$$\mathbb{I}_2 = \iint dA \; |\mathbf{x}\rangle\langle\mathbf{x}|, \tag{2.32}$$

where $|\mathbf{x}\rangle$ is a basis state in position space. We find the expression of Eq. 2.31 in position space as follows:

$$I(x, y) = \langle\Gamma|\mathbb{I}_2|\Psi\rangle, \tag{2.33}$$

which, when expanded, becomes:

$$I(x, y) = \iint dA \; \langle\Gamma|\mathbf{x}\rangle\langle\mathbf{x}|\Psi\rangle = \Gamma^*(x, y)\Psi(x, y). \tag{2.34}$$

Once again, we observe $I(x, y)$ in the Fourier plane by passing it through a lens. This is equivalent to computing the Fourier transform of $I(x, y)$

$$\mathcal{I}(k_x, k_y) = \mathcal{F}\{I\}(k_x, k_y) = \iint dA \; \Gamma^*(x, y)\Psi(x, y)\exp[i(k_x x + k_y y)]. \tag{2.35}$$

Measuring the on-axis intensity, we obtain

$$\mathcal{I}(0,0) = \left| \iint dA \; \Gamma^*(x,y)\Psi(x,y) \right|^2 \propto \delta_{\Gamma^*,\Psi}. \tag{2.36}$$

This shows that one would measure a non-zero on-axis intensity if and only if the functions Γ and Ψ are the same. Physically this implies that the q-plate used as a decoder must have the same topological charge as that of the encoder, **and**, the polarisation measured must also be identical to that of the beam before the encoder.

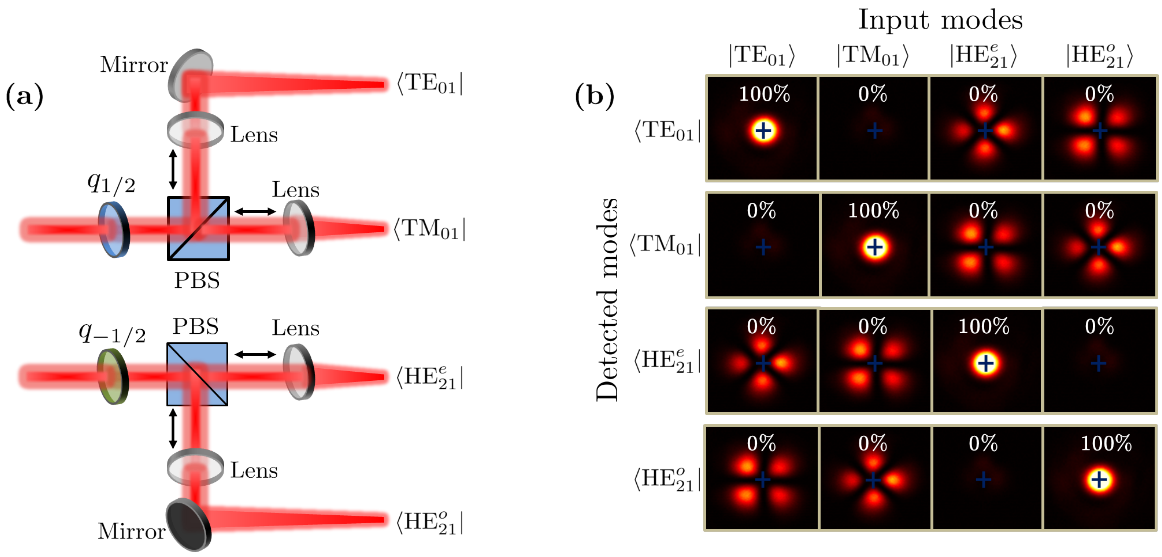

Figure 2.8: Experimental detection of vector vortex modes. (a) the q-plates together with the polarising beam splitters serve as decoders and the vector mode decomposition is completed at the Fourier planes of the lenses. (b) shows the power distribution of the on-axis intensity signal for the four vector modes.

Figure 2.8**(a)** shows the experimental setup that performs the modal decomposition of vector vortex modes. A q-plate with $q = \pm 1/2$ together with a polarising beam splitter (PBS) were used to project the input beam onto each of the four basis vector states. The vector mode decomposition was then completed by measuring the on-axis intensity in the Fourier plane. From the power distribution of the signal shown in Fig. 2.8**(b)**, the absence of modal crosstalk due to, e.g., turbulence in free-space or bends, stress and perturbations of the refractive index in fibres, demonstrates the effectiveness of the technique. Furthermore, this vector mode decomposition would allow the characterization of communication channels employing modes of this particular basis set or higher order VV beams - provided of course that the appropriate

q-plate is used to (de)encode. We will apply this technique to the characterization of optical fibres and atmospheric turbulent channels.

2.3 State tomography of vector vortex modes

Consider the following expression of a particular vector vortex beam (VVB)

$$|\Psi\rangle = |\ell = -1\rangle|L\rangle + |\ell = 1\rangle|R\rangle. \tag{2.37}$$

This expression, as discussed in Chapter 1 is non-separable because it cannot be reduce to a tensor product the degrees of freedom

$$|\Psi\rangle = |\text{spatial}\rangle \otimes |\text{polarisation}\rangle. \tag{2.38}$$

We argued that such a non-separable classical state could be used to model an equivalent quantum system; we understand that there are limitations to this argument, locality being one of the examples discussed in the previous Chapter. In situations where locality need not be violated, tools used to analyse quantum entangled systems can be applied to classical systems such as vector vortex modes. In terms of future implementations of quantum communication with entangled states, the preservation and dynamics of entanglement in a channel is particularly important. There are various measures used in quantum mechanics for entanglement [66]. Here, we chose the concurrence [67, 68] as our measure of entanglement, computed from the density matrix of the system. In most cases, the density matrix of a system is not directly accessible and therefore needs to be reconstructed. In what follows, we explain a procedure to reconstruct the density matrix of a two-qubit (quantum bit) state.

Given a density matrix ρ of system, a concurrence value $\mathscr{C}(\rho)$ is assigned to the system such that $0 \leq \mathscr{C}(\rho) \leq 1$. A concurrence of 1 means "maximally entangled" while a value of 0 means "no entanglement". To evaluate the degree of entanglement, one needs to obtain the density matrix of the system. This is can be achieved by performing a series of projective measurements onto basis state: a state tomography [69]. The method is as follows: Consider a two-particle state $|\psi\rangle$; the density matrix ρ, is given by:

$$\rho = |\psi\rangle\langle\psi|. \tag{2.39}$$

As vector vortex modes are equivalent to maximally entangled two-qubit states, their density matrix can be expressed in term of Pauli matrices

$$\rho = \frac{1}{4}\sigma_0 \otimes \sigma_0 + \sum_{\substack{n,m=0 \\ n\neq m=0}}^{3} \rho_{n,m}\ \sigma_n \otimes \sigma_m \tag{2.40}$$

where

$$\sigma_0 = \begin{pmatrix} 1 & 0 \\ 0 & 1 \end{pmatrix}; \; \sigma_1 = \begin{pmatrix} 0 & 1 \\ 1 & 0 \end{pmatrix}; \; \sigma_2 = \begin{pmatrix} 0 & -i \\ i & 0 \end{pmatrix}; \; \sigma_3 = \begin{pmatrix} 1 & 0 \\ 0 & -1 \end{pmatrix}. \tag{2.41}$$

In addition to being traceless (except for σ_0), These matrices have an important property. That is:

$$\mathrm{tr}\{\sigma_n \sigma_m\} = 2 \; \delta_{n,m} \tag{2.42}$$

for $n, m = 1, 2, 3$. This property allows one to compute the entries of the matrix $\rho_{n,m}$ as follows:

$$\rho_{n,m} = \frac{1}{4}\mathrm{tr}\{\sigma_n \otimes \sigma_m \; \rho\} \tag{2.43}$$

We can express the tensor product $\sigma_n \otimes \sigma_m$ as a superposition of eigenstates with the corresponding eigenvalues as follow:

$$\sigma_n \otimes \sigma_m = \sum_{\substack{n,m=0 \\ n \neq m=0}}^{3} \lambda_{n,m} |u_{n,m}\rangle\langle u_{n,m}| \tag{2.44}$$

where $|u_{n,m}\rangle \in \mathcal{H}_\infty \otimes \mathcal{H}_2$ are the eigenstates and $\lambda_{n,m}$ the corresponding eigenvalues.

Physical density matrices have three main properties: they are normalisable (unit trace), Hermitian and positive semi-definite. Substituting Eq. 2.44 into Eq. 2.43, one obtains an expression of the coefficient $\rho_{n,m}$ as projections of the density matrix onto the space of the various OAM-polarisation eigenstates

$$\rho_{n,m} = \frac{1}{4}\mathrm{tr}\left\{ \sum_{\substack{n,m=0 \\ n \neq m=0}}^{3} \lambda_{n,m} |u_{n,m}\rangle\langle u_{n,m}| \; \rho \right\} = \frac{1}{4} \sum_{\substack{n,m=0 \\ n \neq m=0}}^{3} \lambda_{n,m} \langle u_{n,m}|\rho|u_{n,m}\rangle. \tag{2.45}$$

This yields a total of 16 projective measurements, one needs to perform to obtain the density matrix, from which the concurrence, the degree of entanglement, is computed as follow

$$\mathscr{C}(\rho) = \max\{0, \sqrt{\lambda_1} - \sqrt{\lambda_2} - \sqrt{\lambda_3} - \sqrt{\lambda_4}\} \tag{2.46}$$

where λ_i are the eigenvalues arranged in decreasing order of the Hermitian matrix

$$R = \sqrt{\sqrt{\rho}\tilde{\rho}\sqrt{\rho}} \tag{2.47}$$

where $\tilde{\rho} = (\sigma_2 \otimes \sigma_2)\rho^*(\sigma_2 \otimes \sigma_2)$ and ρ^* is the complex conjugate of the density matrix ρ [68].

Despite the elegance of the method, it is highly affected by statistical fluctuations that stem from the probabilistic nature of the projective measurements. Density matrices measured in this manner often violate three fundamental properties of physical density matrices: normalizability, hermiticity and positive semi-definiteness [70]. Normalizability ensures that probabilities sum to unity, hermiticity guarantees that the eigenvalues of the density matrices, which are linked to direct observables, are real. Positive semi-definitess constrains the eigenvalues to the interval $[0, 1]$. To mitigate the effects of fluctuations, we use an over-complete set of measurement based on mutually unbiased bases (MUBs), which has been shown by Wooters and Fields to optimise the determination of a quantum state [71]. Mathematically two orthonormal bases with dimensionality d $\{|u_1\rangle, \cdots |u_d\rangle\}$ and $\{|v_1\rangle, \cdots |v_d\rangle\}$ are said to be mutually unbiased if they satisfy the following equation

$$\langle u_i|v_j\rangle = \frac{1}{\sqrt{d}} \tag{2.48}$$

For prime dimension d there exist a maximum of $d + 1$ MUBs [71]. For $d = 2$, the 3 MUBs in both OAM and polarisation can be constructed from normalised superposition of the eigenstates with a phase shift between the superposed states [72]. For OAM and polarisation eigenstates these states are located on the equator of the Bloch and Poincaré spheres, thus making a total of three two-dimensional MUBs for each DoF. In the case of vector vortex beams, projections of the state on the 6 basis states of each DoF, extends the number of tomographic measurements to 36 instead of 16.

The reconstruction of the density matrix is achieved by first generating a physical density matrix. This can be thought of as the null hypothesis. Then using a maximum likelihood estimation, the measured density matrix is reconstructed and optimised with respect to the null hypothesis by the complementary projection onto the MUBs. Figure 2.9**(a)** shows the experimental realisation of the state tomography. The projections of the input beam, a $|\mathrm{TM}_{01}\rangle$vector vortex mode, are achieved using a wave plate and a spatial light modulator (SLM). The SLM modulates one of the linear polarisation states (horizontal in our setup) in the diffraction orders. As such, it acts as a horizontal linear polariser in this particular setup. The OAM projections were performed by modulating the incident beam with holograms of the pure OAM states (the poles of the OAM Bloch sphere with $\ell = \pm 1$) and the mutually unbiased superposition states on the equator. The polarisation projections were performed using a wave plate; a quarter-wave plate for the projections on the pure states (poles of the Poincaré sphere) and a half-wave plate for the projections on the MUBs on

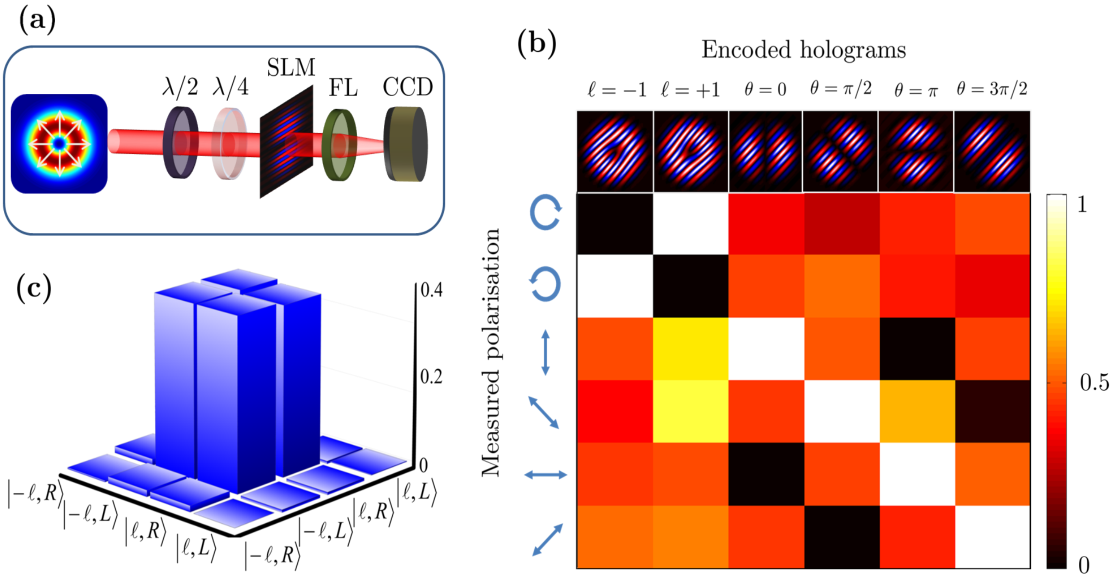

Figure 2.9: State tomography of a $|\mathrm{TE}_{01}\rangle$vector vortex mode. **(a)** shows the experimental setup to perform the projective measurements onto the OAM and polarisation bases. the input beam is passed through a wave-plate to perform the polarisation projection and a SLM where the holograms of the OAM states are encoded. The output is viewed on in the Fourier plane of the lens with a CCD camera. **(b)** shows a summary of the different OAM and polarisation projections. **(c)** shows the reconstructed density matrix.

the equator. The 36 measurements are summarised in Fig. 2.9**(b)**. Based on this measurements, the density matrix was reconstructed as shown in Fig. 2.9**(c)**. Using Eq. 2.46 we obtained a concurrence of 0.97 ± 0.01.

2.4 Conclusion

In this Chapter, we have demonstrated experimental techniques to tailor optical fields to carry digital information. We discussed two flavours of optical modes in the paraxial regime: a scalar type and a vector type. We demonstrated theoretically and experimentally the generation and detection of these optical modes through manipulation of the dynamic and geometric phase.

Firstly, we showed that the dynamic phase can be controlled by varying the thickness of the refractive index of an optical element in order to create a particular mode. This can be achieved statically using spiral phase plates, or dynamically using spatial light modulators. We demonstrated the efficacy of dynamic phase modulation in an experimental setup using SLMs. using digital holograms, we created optical modes carrying quantized OAM charge per photon, and detected them in free space with unit purity.

Secondly, the geometric phase has been shown to arise from the spatially varying anisotropy of phase plates. We showed that this phase can be controlled in order to produce optical modes that carry digital information in the form of vector vortex modes, that exhibit similar non-separability to entangled qubits states. Though we discussed active and passive methods to generate vector vortex modes, we focused on a passive method employing q-plates that couple polarisation to OAM. Using q-plates with topological charge $\pm 1/2$, we built an experimental setup demonstrating the generation of vector vortex modes within the subspace of $|\ell| = 1$. We showed the purity of the modes by detecting them without modal crosstalk in free space.

Finally, we explored the non-separability of vector vortex beams. We demonstrated this relation between the entangled DoFs by showing that measurements on one of the DoFs, determined the state of the other DoF. As this behaviour can be likened to that of quantum entangled systems, we employed measured of quantum entanglement, namely the concurrence, to characterize these seemingly classically entangled systems. The concurrence, in the case of vector vortex modes, quantify the non-separability and distinguishes between scalar and vector modes: a concurrence of 1 signifies purely vector modes (non-separable) and a concurrence of 0 signifying scalar mode (separable). We demonstrated the steps to follow in order to obtained the concurrence: this involved the computation of the density matrix from an optimised state tomography based on mutually unbiased bases of OAM and polarisation.

In the next Chapters, we will use the above techniques that we have developed to characterise communication channels and demonstrate information transfer through various media.

Chapter 3

Communicating with spatial modes

In this Chapter, we explore the potential of spatial modes for communication through experimental optical links we have built in our laboratory. We study the transfer of information through free-space and optical fibres, as these are the two media of choice in optical communication. We demonstrate an increase in information capacity by two orders of magnitude by multiplexing scalar modes over multiple wavelengths channels. Using the wide mode space available, we demonstrate information transfer in the channel by sending and reconstructing data in the form of pictures. Next, we focus on the so-called *last mile* problem: how does one move data from one medium, optical fibre for example, to another one (say free space) without information loss? One key point in this problem, particularly when using spatial modes, is mode matching at the interface between the media, as this affects the transmission. We thus use eigenmodes of both free space and fibres to demonstrate information transfer in a free-space - fibre optical link. The fiber used here is a custom-made 1.5 m long graded index fiber with a 9.5 μm core diameter; this type of fiber supports eigenmodes of the Laguerre-Gaussian type which, are also eigenmodes of free-space.

3.1 Introduction

Communication in its various forms requires signals or patterns that can be distinguished from one another. The more signals or patterns are available, the more one can encode. The same logic applies to spatial modes of light: more distinct modes implies higher encoding capabilities. In the age of digital communication, this distinction should preferably be a single integer number, or a combination of integers. Thankfully, spatial modes already have that distinction built in their structure. The Laguerre-Gaussian mode set discussed in Chapter 1 is a perfect example, labelled with a radial index p and an azimuthal index ℓ. In addition, the LG modes are all orthogonal to each other in the radial and azimuthal indices, making them suitable to carry digital information.

The azimuthal DoF ℓ, associated with OAM, has been, to our knowledge, the centre of all research in communication for various reasons: OAM is a well defined (quantized at the quantum level) property of some optical modes such as LG modes, making it suitable for encoding information at both the classical [13, 73, 74] and quantum level for more secure communication [75, 76]. Furthermore, shaping a light field by complex amplitude modulation, as discussed in the previous Chapter, can a very lossy process depending on the technique and the modes generated [77]. The detection is difficult as well: it requires a precise match in size between the incident field and the decomposing hologram [78].

Despite their orthogonality, spatial modes are susceptible to modal crosstalk: an energy transfer from one mode to another. At the quantum level, this translates into photons scattering into different eigenstates. This is due to perturbations caused by the medium of propagation. A highly perturbing medium thus significantly corrupts the information encoded and limits the ability to multiplex with acceptable levels of purity. Classically, the crosstalk is evaluated by measuring the relative power distributed among eigenmodes when a single mode propagates through a channel. For spatial modes, this measurement is performed by modal decomposition as described in Chapter 2.

In this Chapter, we want to demonstrate that spatial modes can be used in communication to increase the bandwidth of a channel. We focus on two important aspects: the nature of the link and the available mode space. Though many studies have been conducted on the transport of spatial modes in free-space or optical fibres, not much has been done in composite free-space-fibre links. Some notable studies include the implementation of code division multiple access signals [79] and WDM [80] in composite free-space- fibre links. Here we demonstrate the use of spatial modes for bandwidth increase in composite free-space-fibre link. With regards to the available mode space, we demonstrate an increase of 2 order of magnitude using for the first time both DoFs of LG modes; these are the radial and azimuthal indices.

3.2 Free-space-fibre optical link

The complexity in using spatial mode to communicate through dissimilar media such as free space and optical fibres arises from the fact that the solutions to the paraxial Helmholtz equation differ for both media. In free space, these solutions depend on the symmetry of the medium [81] while in fibres they depend on the structure of the refractive index of the core [29]. The most commonly known type of fibre is one with a step index structure as shown in Fig. 3.1(a). The core has a higher but constant refractive index compared to the cladding, guiding light by total internal reflection. In the fibre, the solutions to the paraxial Helmholtz equation

$$\left(\nabla^2 + n^2k^2 - \beta^2\right) E(r,\phi) = 0, \tag{3.1}$$

can be approximated by the linearly polarised (LP) modes whose optical field is given by

$$E_{\ell,p} = R_{\ell,p}(r)\Phi_\ell(\phi), \tag{3.2}$$

where

$$R_{\ell p}(r) = \begin{cases} J_{|\ell|}\left(\frac{ur}{a}\right)/J_{|\ell|}(u) & \text{for } r < a \\ K_{|\ell|}\left(\frac{wr}{a}\right)/K_{|\ell|}(w) & \text{for } r \geq a \end{cases} \tag{3.3}$$

$$\Phi_\ell(\phi) = \begin{cases} \cos(\ell\phi) & \text{for even modes} \\ \sin(\ell\phi) & \text{for odd modes,} \end{cases} \tag{3.4}$$

where a is the radius of the core, J_ℓ is the ℓth order Bessel function, K_ℓ is the ℓth order modified Bessel function, u and w are a normalized propagation constants

$$u = \sqrt{k^2 n_{co} - \beta^2} \tag{3.5}$$

$$w = \sqrt{\beta^2 - k^2 n_{cl}}, \tag{3.6}$$

where n_{co} and n_{cl} are the refractive indices of the core and the cladding respectively, and $k = 2\pi/\lambda$. The intensity patterns of some LP modes are shown in FIg. 3.1(b), using the label $\mathrm{LP}_{\ell,p}$ for each mode. These LP modes are however not eigenmodes of free-space and would not be suitable for a free-space - fibre composite link.

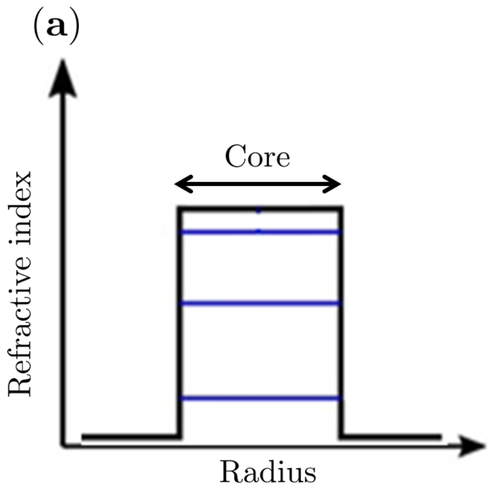

Figure 3.1: Step index fibre characteristics. (a) shows the refractive index profile of the core and (b) the first five guided modes of the set of $LP_{\ell,1}$ modes

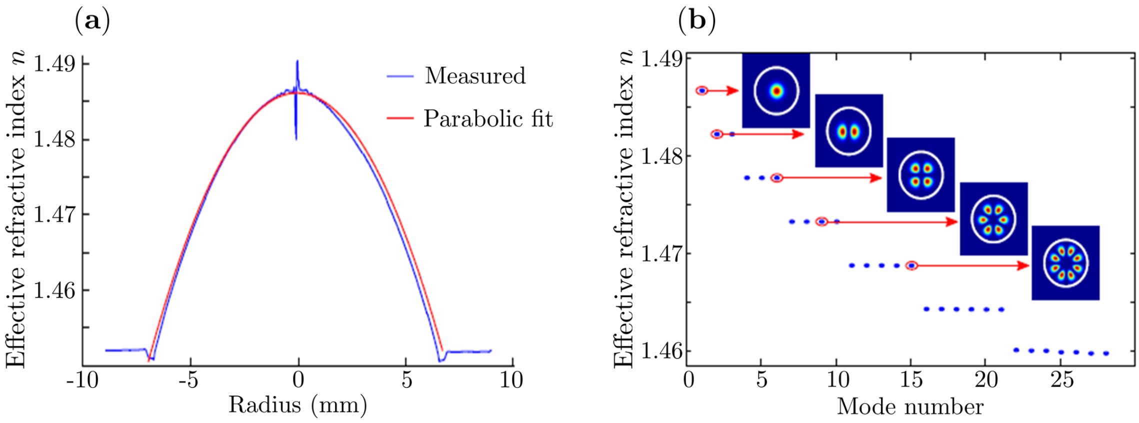

Figure 3.2: Graded index fibre characteristics. (a) shows the refractive index profile measured at the preform and the parabolic index fit. (b) shows the fibre eigenmodes spectrum. The blue dots represent modes in particular mode groups. The insets depict the mode profile inside the fibre (white circle)

We proposed that by modifying the refractive index structure, one can design a fibre that can support eigenmodes of free-space. That is the case for graded index fibre (GIF) having a parabolic core index structure as shown in Fig. 3.2(a) given by

$$n^2(r) = n_{co}^2 \left(1 - 2\Delta r^2\right), \tag{3.7}$$

where $\Delta \cong (n_{co} - n_{cl})/(a\, n_{co})$ in the paraxial regime. These fibres called graded index fibres, support modes with Laguerre-Gaussian envelop and petal-like patterns that can mathematically be expressed as

$$\begin{aligned} LG^e_{p,l} &= A_{p,l}(r,z)\cos(\ell\phi) = A_{p,l}(r,z)\left[\exp(i\ell\phi)+\exp(-i\ell\phi)\right] & (3.8)\\ LG^o_{p,l} &= A_{p,l}(r,z)\sin(\ell\phi) = A_{p,l}(r,z)\left[\exp(i\ell\phi)-\exp(-i\ell\phi)\right], & (3.9)\end{aligned}$$

where $A_{p,l}(r,z)$ is the LG radial profile as defined in Eq. 1.8 in Chapter 1. Note that these fibre modes are equivalent to superpositions of the conventional cylindrically symmetric LG modes discussed in Chapter 1. Also note the intensities of these modes are identical to those of the LP modes supported by step index fibres. It has recently been shown that LP modes can be approximated by appropriately adapted LG modes sets [82]. This raises the possibility of utilising LG modes in a composite link that include step index fibres. Modes with identical constant $C = 2p + \ell$ experience the same effective refractive index in the fibre, leading to the formation of mode groups. With all the modes within a group being degenerate, this further increase the probability of mode coupling within a group.

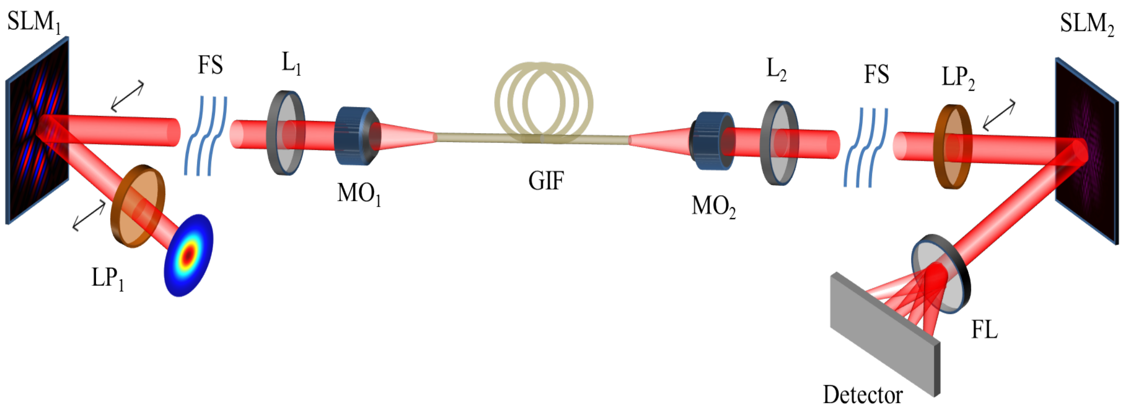

Figure 3.3: Experimental setup used to demonstrate information transfer across a 4.5 m composite communication link. Light from a He-Ne laser ($\lambda = 633$ nm) was passed through a linear polariser (LP_1), shaped using SLM_1 to generate the desired modes, then propagated through 1.5 m free-space (FS), followed by 1.5 m fibre and finally another 1.5 m FS to be decoded by SLM_2. The lens L_1 and the microscope objective MO_1 served to inject the modes in the fibre which were then expanded using MO_2 and L_2, then horizontally polarised with LP_2. The modes were demultiplexed by encoding all five modes onto SLM_2, but with different diffraction gratings. The local on-axis intensity was measured at each of the five different positions on the detector, which was placed at the Fourier plane of the lens (FL).

We proceeded to build the optical link shown in Fig. 3.3. We shaped light from a He-Ne laser ($\lambda = 633$ nm) using a spatial light modulator (SLM_1). This SLM was used as an encoder for the LG modes that were propagated through a link consisting of 1.5 m of free-space, followed by 1.5 m of graded index fibre and finally 1.5 m of free-space. The output of the link was analysed by modal decomposition using SLM_2 and viewed on a camera detector place at the Fourier plane. of the Fourier lens. At a wavelength of 633 nm, there are 28 modes supported by this fibre, calculated using the vector finite difference modesolver described in [83]. The ordering of the modes within a group follows two rules: modes with higher ℓ occupy higher position and even modes precede odd modes. The ordering is as follow: LP_{01}, LP^e_{11}, LP^o_{11}, LP_{02}, $\cdots$, LP^o_{61}. Figure 3.4 shows significant amounts of modal coupling within and outside of the mode group. A closer observation revealed that this coupling is even more pronounced for modes with $p \neq 0$. We also noted that higher mode groups suffered important losses in signal intensity. This is due to light being lost in the cladding of the fibre as the size of the modes increases. We concluded that using all 28 modes to transmit information would not be ideal as the signal would be highly distorted by the fibre due to the significant amount of inter-modal crosstalk.

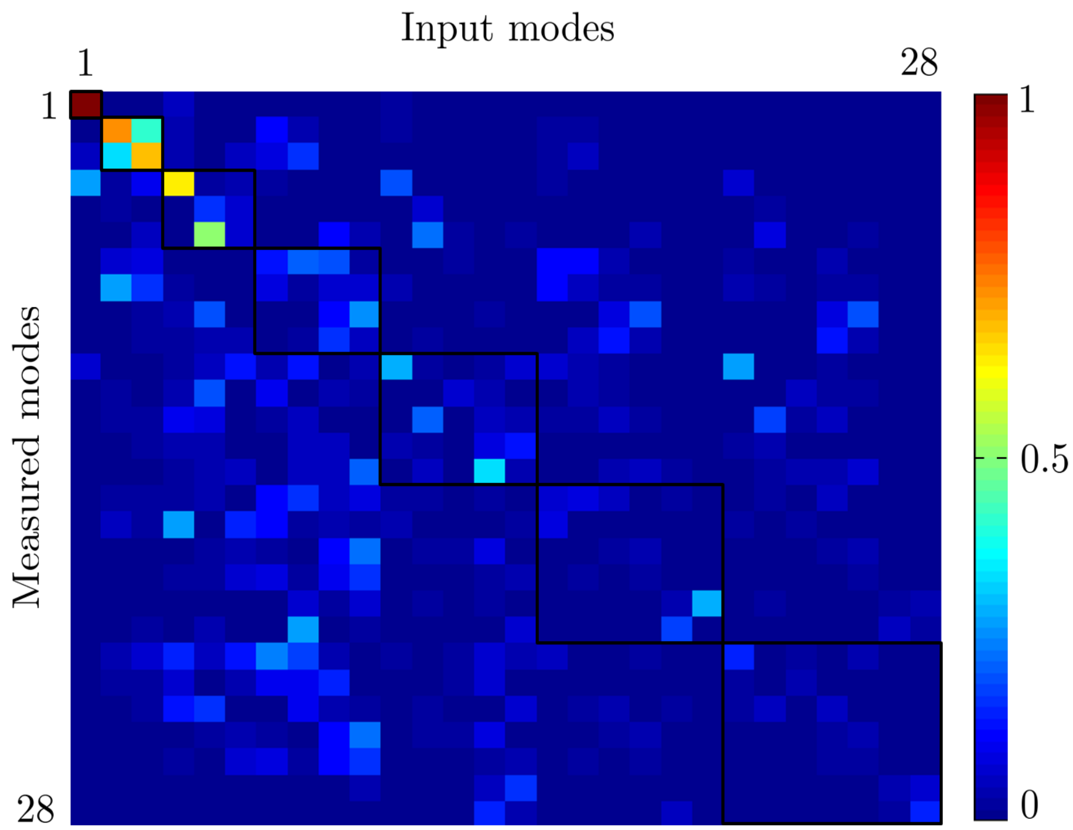

Figure 3.4: Modal crosstalk measured for a 9.5 μm core diameter and 1.5 m long graded index fibre. The black squares delimits the mode groups

Based on the losses in higher mode groups, as well as the crosstalk from modes with non-zero p index, we re-evaluated the amount of coupling. this time for modes from the first five modes groups having $p = 0$. The results shown in Fig. 3.5(a) shows the emergence of peak signals within modes groups and less significant inter-modal coupling. In some cases, we noted that the modes injected in the link completely coupled to other modes. The relative strengths of the signals within mode groups did not however, allow us to use all the modes in this narrowed mode set. Previous research has shown that increasing the eigenvalues spacing reduces modal coupling [84, 85]. Using this finding, we further narrowed our mode space to 5 modes based on the strength of the signal measured and the coupling. Figure 3.5(b) shows the coupling strength in dB between the modes chosen. Note that the null diagonal represent states of zero coupling. Based on the strong coupling measured for the third, fourth and fifth modes prepared, we considered the detected modes to be identical to the prepared ones.

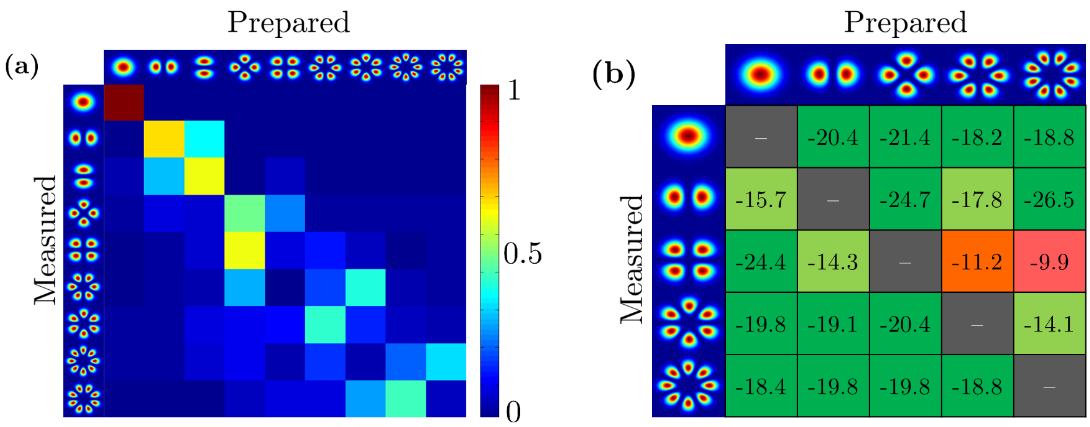

Figure 3.5: (a)The crosstalk matrix for the first five mode groups of a graded index fiber, excluding the radial modes.(b) The crosstalk matrix in dB for the five LG modes chosen to transmit data through the link

Having now characterized the modal coupling in the communication channel, we proceeded to use to send data through it in the form of a 30×30 pixel image of Einstein. We prepared a gray-scale image with five shades of gray, with each shade assigned to one of the modes we previously selected (prepared modes from Fig.3.5(b)) as depicted in Fig. 3.6. The pixels on the encoded image were read successively, with a particular mode send through the link as a particular pixel colour was read. Using a spatial light modulator, each mode sent through the link was analysed by modal decomposition with holograms of the modes previously selected for detection

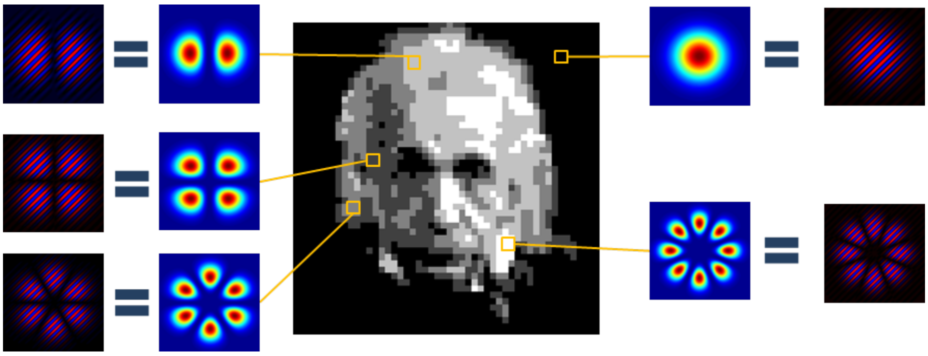

Figure 3.6: A gray-scale image of Einstein, consisting of 30 by 30 pixels, was transmitted over the communication link, using five different modes to represent five different gray levels. Each transmission represented a single pixel of the image.

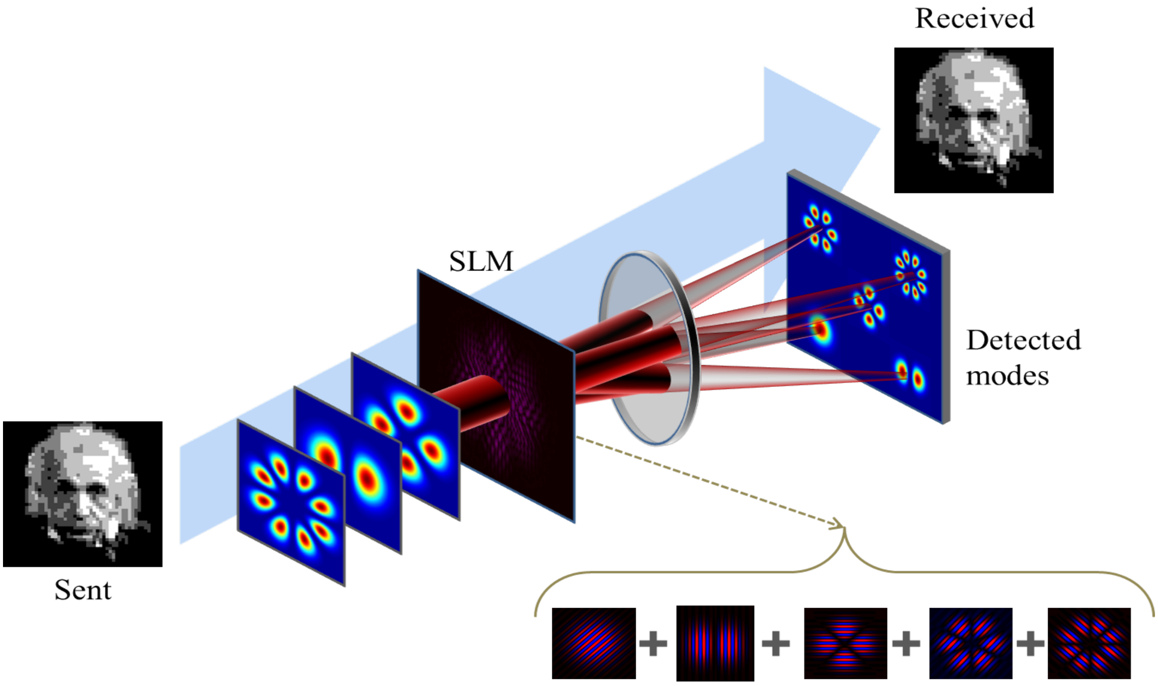

Figure 3.7: Five different LG modes were used to encode the gray-scale image, which was then demultiplexed using another five LG modes. Each mode was encoded with a different diffraction grating so as to spatially separate the detected modes. The on-axis intensity at each spatial position was on a camera.

(measured modes from Fig.3.5(b)) as illustrated in Fig. 3.7. On the detector, among the 5 detection position for the five modes, that with the highest on-axis intensity signal defined the colour of the pixels in the reconstructed image. In this way, we achieved a 100% reconstruction. Note that this has been possible because of two key point in the experimental procedure: one, we carefully selected the encoding and decoding mode sets to minimise modal coupling. Two, we selected only the position with the highest signals among the five on the detector. In this instance, this approach to the measurement is entirely valid as choosing the maximum value is equivalent to applying a threshold to the measurements. This however would not work in a multiplexing setup as signals for more than one position would be required. The threshold would have to be decreased to an appropriate value.

The purpose of this composite link was to simulate a large scale last mile link. The bottleneck in last mile link is the inability to extract information at high rate at the receiver's end. In the above, we have shown that by characterising the channel, one can select an optimum mode set to encode information. To increase the data rate at the receiver's end in a last mile link, one needs successfully implement MDM with low enough thresholding. In this way, one would demonstrate an N-fold bandwidth increase in last mile link employing N spatial modes. To take full advantage of the mode space available for encoding, one will also need to use modes with non-zero p index, which has never been done. Next, we demonstrate a link in which, for the first time, LG modes with radial and azimuthal indices are used to achieve a 100+ increase in available bandwidth.

3.3 Mode-division multiplexing with over 100 modes

Utilising spatial modes in communication requires an optimum use of the available modes. To this end, multiplexing techniques can be used to take full advantage of the orthogonality of spatial modes such as LG modes; this is referred to as mode-division multiplexing (MDM): multiple spatial modes are simultaneously sent through a single communication channel. This technique has been demonstrated in both free space [86, 14, 87, 88] and fibres [15, 89–91] using OAM, achieving speeds of the order of terabits per second. A common trend in communication with spatial modes, is the lack of interest in the radial dependence of these modes, an unexploited degree of freedom. For LG modes, this dependence is governed by a radial index p, that is well defined and thus suitable to carry digital information. The orthogonality of the LG modes ensures that information encoded in the radial and the azimuthal index can be unambiguously recovered under ideal conditions (no perturbation).

As discussed earlier, detecting radial modes using holographic modal decomposition is lossy and is very sensitive to alignment and mode size. In a free-space link through a turbulent atmosphere, a beam is subjected to aberrations that affect the mode size and changes the axis of propagation, making the detection all the more difficult. These effects could be accounted when designing the link as it has been reported for OAM modes [92, 93].

Making use of the radial dependence of spatial modes definitely holds the potential to increase the capacity of optical links. We demonstrated this by encoding information in both the radial and azimuthal indices of LG modes. We built the optical link shown in Fig. 3.8. An Argon-ion laser, emitting a multicoloured light with spectral lines at 418, 488 and 514 nm, illuminates a spatial light modulator (SLM-1) that act as the modal encoder. On each of the three beams, modes within the LG set with $p \in (0, 4)$ and $\ell \in (-3, 4)$ excluding $\ell = 0$ were encoded; a total of 105 modes over the three wavelengths by designing wavelength independent holograms [94]. The grating for all the modes encoded on a single wavelength was constant. Using a 4f projection system, the plane of SLM-1 was projected on SLM-2 where the beams were demultiplexed. Each of the beam was demultiplexed with the sum of all the 35 encoding modes, each having a different grating to place the outputs at different detection position on the CCD camera.

Given an encoded mode $U(x, y)$ on wavelength λ, the on-axis measured by a detector located at position j on the CCD camera is given by

$$|I_{\lambda,j}(0,0)|^2 = |\langle \mathrm{LG}_j | U \rangle \exp(i\theta_j)|^2 \tag{3.10}$$

where $j \in (1, 35)$ labels the 35 decomposing LG modes and θ_j the associated phase grating. Each detected position therefore corresponds to a particular detected LG mode.

The presence of strong 1:1 correlation between the prepared and measured modes as shown in Fig. 3.9, characterised by the strong signals along the diagonal, evidently show that: we can use all 105 modes for encoding, and by applying an appropriate threshold, we can achieve successful MDM with high enough purity to further increase the channel capacity.

To support our claim, we sent data through the link using various encoding technique. The first and simplest one is called single bit encoding. It is the same technique we previously used to encode information in our composite link: we prepared images with a 105 shades of gay and assigned to each shade a particular mode that was then sent through the link as the images was read at the encoding stage. The reconstructed image was obtained by successively reading the maximum of the 105 outputs and assigning the corresponding colour to the pixel reconstructed. Our results are shown

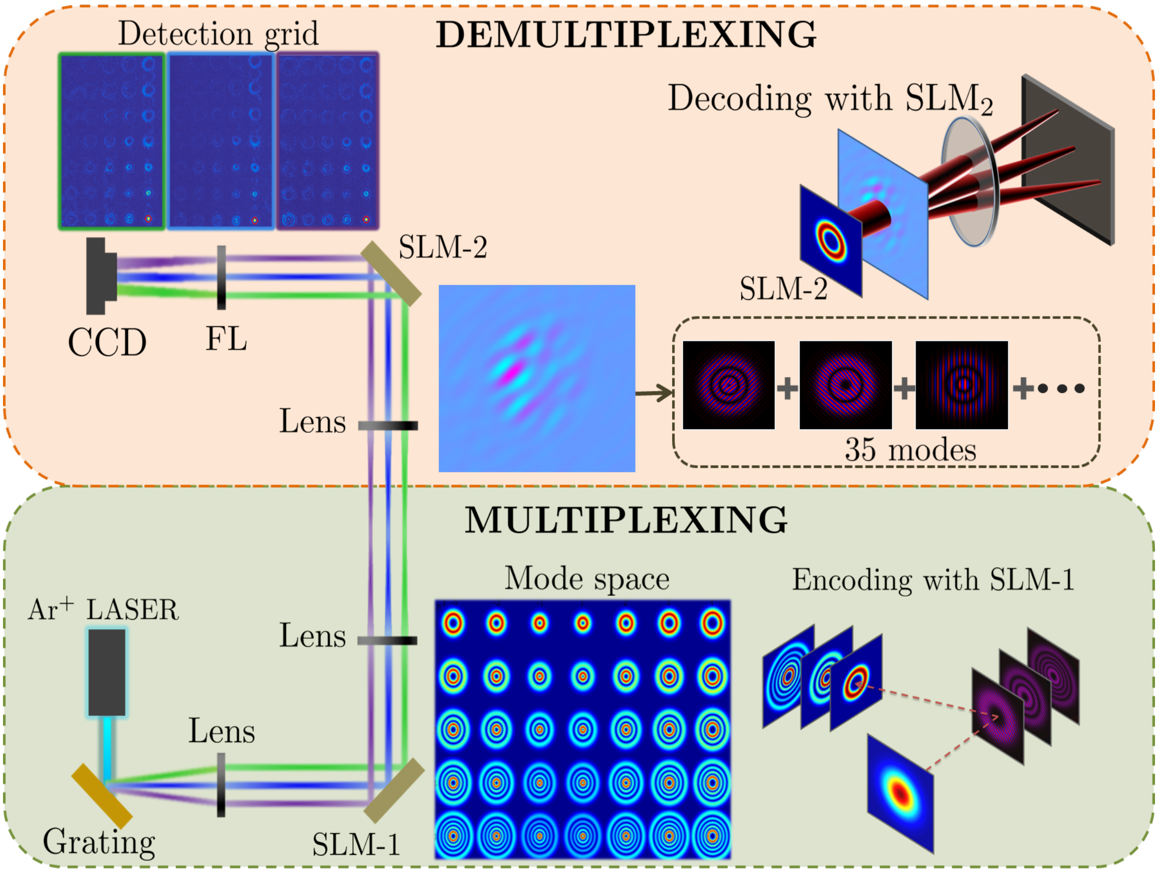

Figure 3.8: Experimental optical link employing mode-division multiplexing. Multi-coloured light form an Argon-ion (Ar^+) laser was split using a grating, into three laser beams with spectral lines at 418, 488 and 514 nm. The beams were collimated and directed on SLM-1 which served and the modal encoder to multiplex LG modes, each beam having a modal capacity of 35, for a total of 105 modes. The three beams were then directed to three sections of SLM-2 that acted as the decoder. On each section, the sum of holograms from the 35 encoded modes, each having a different grating, was displayed to demultiplex each of the three beams by modal decomposition. The outputs were observed at the Fourier plane of a Fourier lens (FL) placed after SLM-2.

in Fig. 3.10. We reconstructed 50×50 pixel images of Newton and Planck with a correlation efficiency (CE) of 90% and 85% respectively.

By efficiently using the large mode space available, we can not only encode images, but also in colour. For this, we used a second technique which we call RGB encoding. This time, each colour pixel was represented as a superposition of shades of red (R), green (G) and blue (B). Conveniently, we had a laser that produced three colours. As such, we assigned each of our three beams to one of the RGB colours, and the shades of each colour was encoded by the 35 modes used on each laser wavelengths. The reconstruction of the shades of each of the three RGB colours was as in the case

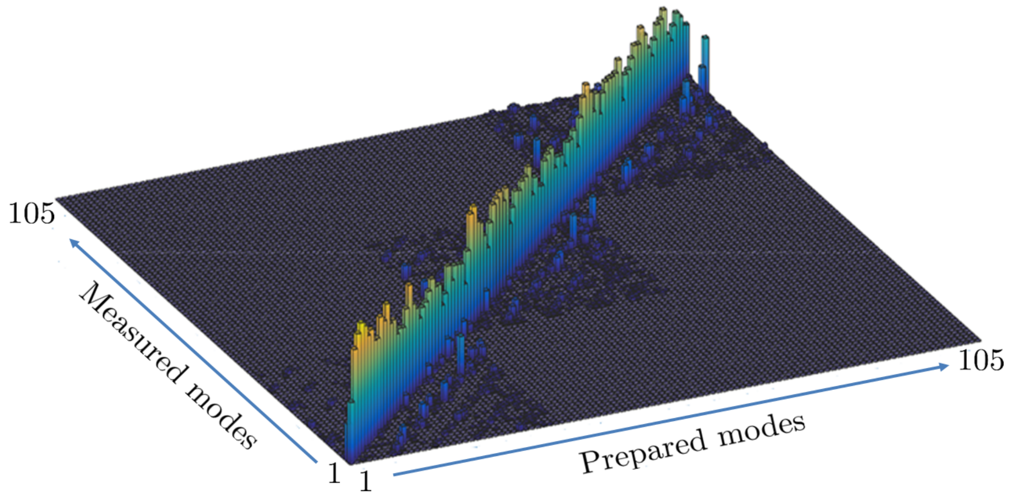

Figure 3.9: Inter-modal crosstalk measured for the 105 LG modes showing a strong 1:1 correlation between the prepared and measured modes.

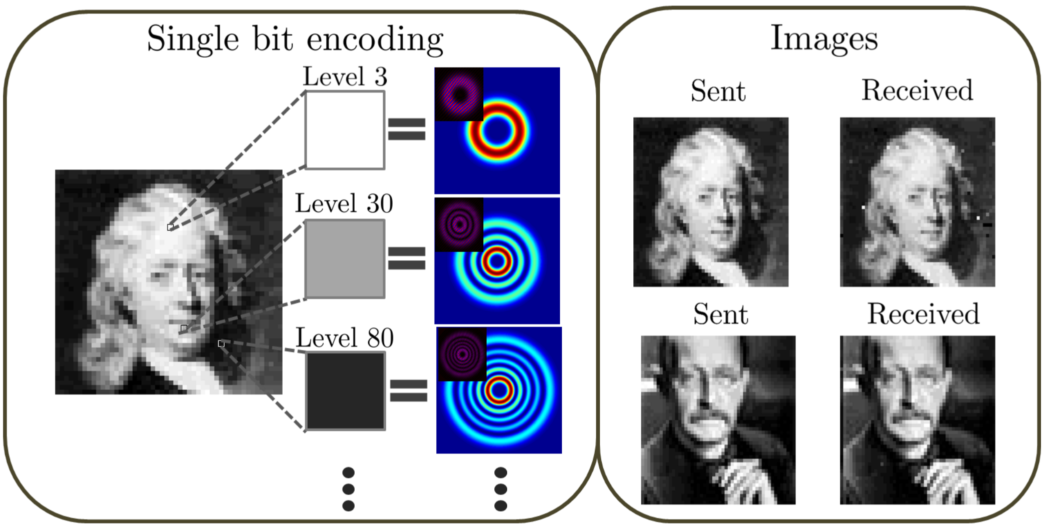

Figure 3.10: Single bit encoding using a 105 mode space. To each of the 105 shades of gray composing the image, a particular LG modes is assigned, together with a particular wavelength.

of single bit encoding and the results are shown in Fig. 3.11. In this case, we had a CE of 82% and 98% with 50×50 images of Lena and the international year of light logo respectively.

Finally, we implemented MDM to increase the amount of bit that could be encoded past the 105 limit we previously had. This allowed us to encoded images with better contrast and in colour. To achieve this, we needed a mere 8 modes for each wavelength. We performed a multi-bit encoding: the shade of each RGB colour was encoded as a

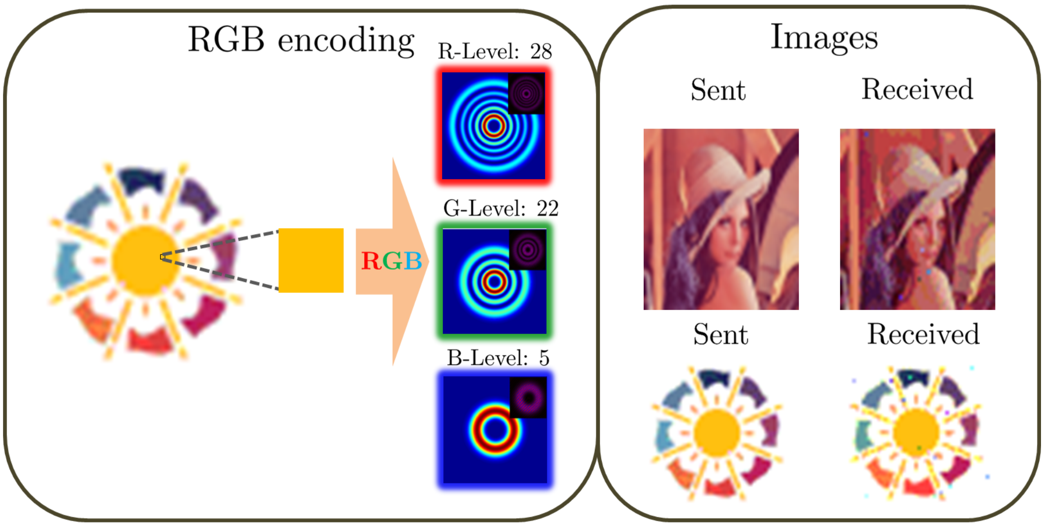

Figure 3.11: RGB encoding using a 105 mode space. Each pixel is a represented as a sum of RGB colours. Each colour is assigned to a wavelength of the Ar^+ laser and the shades of each colour is encoded by 35 modes.

binary sequence that is N-bit long (in this case N=8). In decimal, this means that one can encode the any number from 0 to 255 ($2^N - 1$), effectively increasing the number of bits we could encode from 105 to 256. For this, we chose the 8 modes to represent position in the 8-bit sequence. The detection for the shades of each RGB colour was performed by measuring the relative signals from all 8 positions and applying a threshold; signals above the threshold are considered as one while those below are taken to be zero. With this method, We reconstructed the images shown in Fig. 3.12, with a CE of 96% and 99%, respectively, for the university logo and the rubik's cube.

3.4 Conclusion

We have demonstrated that spatial modes of light have the potential to support the next leap in optical communication, by providing additional channels over which current communication protocols can be used. Recently, this has also been demonstrated with vector vortex beams [95, 96]. Using scalar Laguerre-Gaussian modes, we showed an optical link that utilising 105 spatial channels. We showed that the relative independence of the channels allowed for spatial modes to be multiplexed, thereby increase the channel capacity. Using these spatial modes as bits of information, we transferred data in the link using both space- and mode-division multiplexing. In a noisy channel however, the deleterious effects that arise from of modal coupling

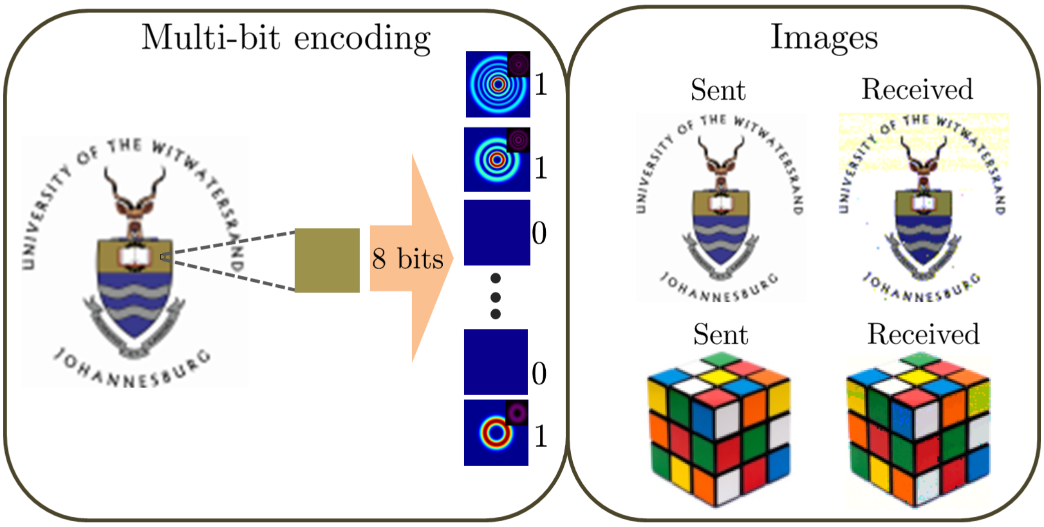

Figure 3.12: Multi-bit encoding using 8 modes. Each pixel is expressed as a sum of RGB colours. The shades of each colour is encoded using an 8-bit long binary sequence, with each position on the sequence assigned to a particular mode. By applying a threshold, one determines the value of a bit in the sequence: if the signal measured from a mode is above the threshold, it is one, else it is zero.

reduces the ability to multiplex spatial modes.This was demonstrated in a composite free-space - fibre link. We characterized the modal crosstalk in the link arising from perturbations caused by the channel, and optimally selected an encoding mode set that mitigates the coupling among the modes. Through this procedure, we showed successful information transfer with unit fidelity. Furthermore, we argued that by an optimally selected mode space would allow for mode-division multiplexing in the future to increase the bandwidth. Note that here, due to the short length scales (1.5 m at most), and the controlled laboratory environment, turbulence effects can be neglected. In the next Chapter, we introduce atmospheric turbulence and study its effects on quantum and classical communication links.

Chapter 4

Quantum transport with classical light

4.1 Introduction

Thus far, we have investigated the use of spatial modes of light for classical communication. We showed that spatial modes provide additional channels that can be multiplexed for increased bandwidth. This increase in information capacity, as we have shown for OAM modes, is evident down to the single photon level. As such, the spatial degree of freedom opens the door to a plethora of applications in quantum communication. Traditionally, polarisation has been used as the DoF of choice in photonic channel for quantum key distribution [97, 27, 98], quantum teleportation [26, 99] or dense coding [100, 101]. In recent research, vector vortex modes have been used in two dimensional quantum key distribution because of their rotation invariance, which is a drawback in polarisation based key sharing [102, 103].

A key property of quantum states that is at the heart of many quantum communication protocol is quantum entanglement [104]. Entangled particles have the fascinating property that knowledge of the quantum states of one particle, instantaneously affects the quantum state of the other entangled particle(s). Though significant progress has been made in using quantum entanglement as a resource for communication, the polarisation DoF limits the level of security and information capacity of photon; this is because the polarisation DoF, unlike the OAM, spans only a two dimensional Hilbert space. As such, each photon can only carry two bits of information. The infinite dimensional OAM space allows for an infinite amount of information to be encoded on a photon. Experimentally, the transport of photons entangled in the spatial DoF has already been demonstrated in the laboratory [75, 105–107], but never on larger scales. To date, this transport has been limited to a few centimetres in optical fibres only [108, 109]. This is because entanglement correlations are fragile. Perturbations from noisy channels, a turbulent atmosphere or an optical fibre for example, cause crosstalk which affects entanglement correlations. Studying the transport of entangled spatial modes thus requires knowledge of the channel which, itself, cannot be accessed without having transported these modes through it, thus the challenge in using the spatial DoF for quantum communication.

To a certain extent, the study of quantum properties does not necessarily require quantum objects [37, 110, 111]. In this instance, the evolution of the entanglement of a bipartite system can be conducted classically with vector vortex modes. These particular spatial modes possess non-separable (or entangled) degrees of freedom: OAM and polarisation. This classically entangled light beams offer the possibility of evaluating the evolution of entanglement through a particular noisy channel using a bright source. In this Chapter, we study the transport of vector vortex modes through two noisy communication channels: an optical fibre and a turbulent atmosphere. The fibre used here was a 5 cm long step-index fiber having a 30 μm core diameter, while the atmospheric turbulence was digitally generated using a spatial light modulator.

4.2 Transport of vector vortex modes through fibres

Multimode fibres are required to transport entangled states spatial modes. However in this type of fibres, modal coupling, the energy exchange among the guided modes, is a major hindrance even after on a few millimetres [112]. Consequently this negatively affects entanglement correlations [108] and detection probabilities. The effect of the fibre on entanglement correlations can be measured through the concurrence of the entangle states.

Recall from Chapter 2 that the concurrence is a measure of the degree of entanglement or non-separability. However, non-separability is not unique to quantum states. We showed in Chapter 1 that vector vortex modes, the true eigenmodes of optical fibres, are formed from a superposition of non-separable OAM and polarisation hybrid states, whose concurrence can also be computed [33]. This makes vector vortex modes ideal to model the evolution of quantum entanglement in fibres.

To study the effect of fibres on the non-separability of vector vortex beams, we built the optical setup shown in Fig. 4.1. Light from a He-Ne laser was modulated in phase and amplitude using a SLM (this was to control the size of the beam injected in the fibre) to produce a horizontally polarised Gaussian beam. Using a half-wave plate and a q-plate, The input Gaussian beam was transformed into a vector vortex beam

$$|U\rangle = A(\vec{r}) \times (|\ell\rangle|R\rangle + \exp(i\theta)|-\ell\rangle|L\rangle) \tag{4.1}$$

where $\ell \in \{-1, 1\}$ is the OAM degree of freedom, $\{R, L\}$ are the right and left circular polarisations and θ is the intra-modal phase shift. The generated vector vortex beam was then injected into a 30 mm multimode step-index fibre with a core radius of 15 μm. The output of the fibre was magnified and directed onto two detection systems: our vector mode detector and our tomography detector.

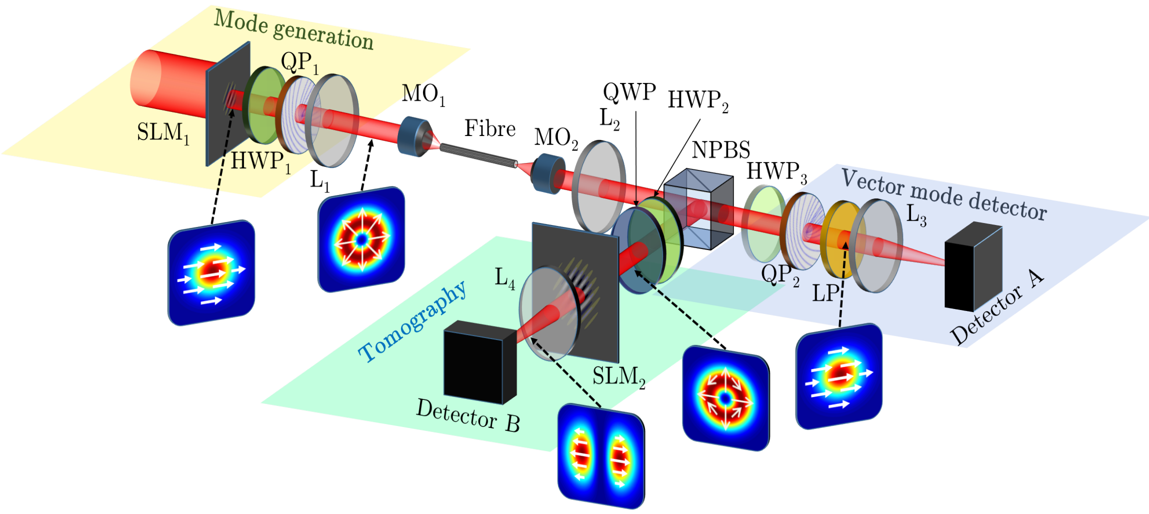

Figure 4.1: Experimental transport of vector vortex beams through a fibre. A beam with flat wavefront was modulated in phase and amplitude using SLM_1 to produce a Gaussian beam that is horizontally polarised. A half-wave plate (HWP) and a q-plate (QP_1) were used to generate vector vortex beams that were then injected into a 30 mm multimode step index fibre with core radius 15 μm using a demagnifying telescope composed of a lens_1 and a microscope objective MO_1. The fibre output was, using MO_2 and L_2, expanded, split using a non-polarising beam splitter (NPBS) and directed onto two detection systems. a tomography detector to compute the concurrence and a vector mode detector to measure the inter-modal crosstalk by modal decomposition.

The first is a vector mode detector that determines the inter-modal crosstalk. As mentioned in Chapter 1, we were interested in the four vector vortex modes of the $|\ell| = 1$ OAM subspace. To demonstrate the effect perturbing effect of optical fibres, we show in Fig. 4.2 the coupling between vector vortex modes with and without the fibre. Using the detection technique for vector modes explained in Chapter 2, we performed a decomposition in the vector basis formed by the four vector modes in the $|\ell| = 1$ subspace. Evidently, the fibre causes the transfer of energy between the modes over a few millimetres as shown in [112]. The crosstalk is so severe that in the case of a $|\mathrm{TE}_{01}\rangle$ and a $|\mathrm{HE}^{o}_{21}\rangle$, the input mode is nearly absent at the output.

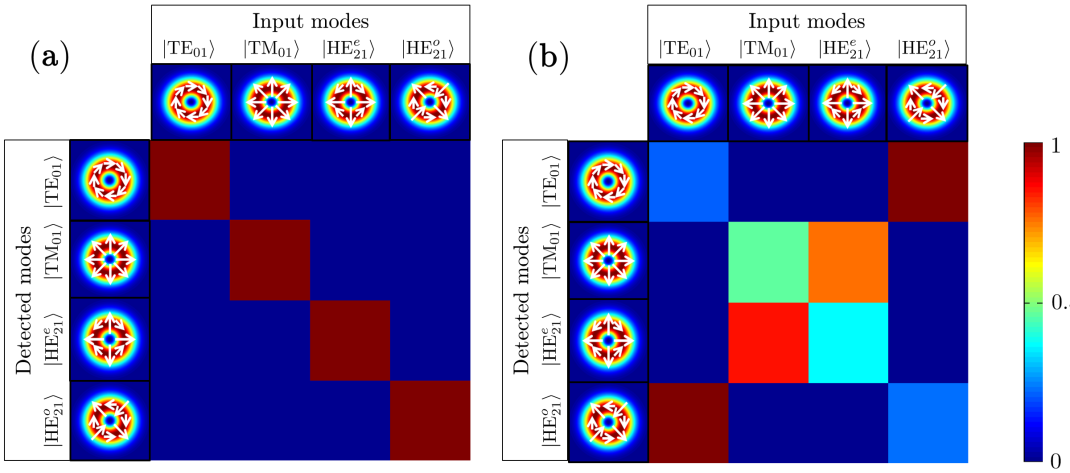

Figure 4.2: Experimental modal coupling among vector vortex modes in the $|\ell| = 1$ subspace in (a) a few centimetres of free space and (b) a 30 mm multimode step-index fibre with core radius 15 μm

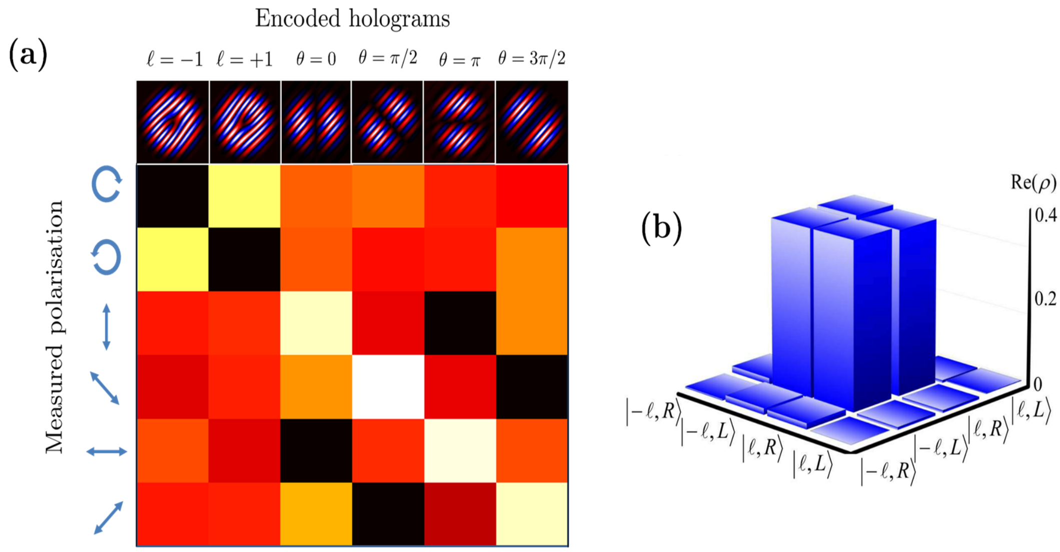

Figure 4.3: Experimental full state tomography of a $|\mathrm{TE}_{01}\rangle$mode. (a) shows the projective measurements into the OAM and polarisation bases, from which (b) the density matrix was reconstructed

The determination of this crosstalk matrix however allowed us to predict the behaviour of a vector mode in the fibre used. The matrix shows that the $|\mathrm{TE}_{01}\rangle$ and

$|\mathrm{HE}_{21}^{o}\rangle$ coupled strongly to each other. As such, we injected a $|\mathrm{HE}_{21}^{o}\rangle$ mode into the fibre and performed a state tomography, described in Chapter 2, of the output beam (a $|\mathrm{TE}_{01}\rangle$ mode according to the coupling matrix). Figure 4.3(a) shows the projective measurements into the OAM and polarisation mutually unbiased bases, which were then used to reconstruct the real density matrix shown in Fig. 4.3(b). Recalling Eq. 2.46, we computed the concurrence as

$$\mathscr{C}(\rho) = \max\{0, \sqrt{\lambda_1} - \sqrt{\lambda_2} - \sqrt{\lambda_3} - \sqrt{\lambda_4}\} \tag{4.2}$$

where ρ is the density matrix and λ_i are the eigenvalues in decreasing order of the Hermitian matrix

$$R = \sqrt{\sqrt{\rho}\tilde{\rho}\sqrt{\rho}} \tag{4.3}$$

where $\tilde{\rho} = (\sigma_2 \otimes \sigma_2)\rho^*(\sigma_2 \otimes \sigma_2)$ and ρ^* is the complex conjugate of the density matrix ρ [68]. We obtained a concurrence value of 0.98 ± 0.01. Also recall that a concurrence of 1 signifies that a composite state in non-separable while a concurrence of 0 signifies that the composite state is separable.

Through this experiment, we have therefore shown classically that the non-separability of vector vortex beams is conserved over a few centimetres of fibres. It is worth mentioning that these classical results are fibre specific. The modal coupling inside fibres is dependent on various parameters, an important one being the size and shape of the core. At a particular wavelength, the size of the fibre core affects the modal capacity of the fibre, making it single or multimode. In addition, due to manufacturing defects and inconsistency, fibres tend to have a slightly elliptical core, causing it to be birefringent. The more elliptical the core is, the higher the birefringence [29]. This birefringence causes a periodic exchange of energy between the polarisation components, with period [4]

$$L(B_m) = \lambda/B_m \tag{4.4}$$

where B_m is the modal birefringence. Thus the coupling effects differ from one fibre to the another. This also makes the modelling of the fibre crosstalk very challenging. Next we look at a relatively simpler, yet very significant case where only one of the entangled degrees of freedom is perturbed.

4.3 Transport of vector vortex modes through atmospheric turbulence

The sharing of information between remote parties has not yet been achieved through free-space using entangled spatial modes. Similarly to optical fibres, it has been shown that a turbulent atmosphere causes the scattering of photons among eigenstates which has deleterious effects on the photons detection probabilities [113], information capacity [114, 115] and entanglement correlations [116, 117]. Here we show that the transport of entangled quantum states can be modelled classically using vector vortex beams. To this end, we will model the situation shown in Fig. 4.4, where Alice sends information to Bob through a free-space turbulent channel. In the quantum picture, she creates two entangled photons by spontaneous parametric down conversion [118] using a non-linear crystal and sends one photon to Bob. In the turbulent channel, the photon sent by Alice is perturbed by the channel, which in affects the quantum correlation between the entangled photons. Equivalently, in the classical picture, Alice send information to Bob through the same channel using a vector vortex beam. The spatial degree of freedom is perturbed by the channel while the polarisation is not. The spatial degree of freedom and the polarisation are equivalent, respectively, to the photon Alice sent and the one she kept. And similarly to the quantum picture, the classical correlations between the DoFs is affected by the channel. In the following, we show that the classical picture accurately models its quantum equivalent.

It has been shown that under the effect of turbulence, the spreading of the OAM spectrum as a consequence of crosstalk, is similar regardless of the mode number [119, 120]. Thus, consider a given vector vortex mode

$$|U\rangle_{\ell}^{in} = |\ell\rangle|R\rangle + |-\ell\rangle|L\rangle. \tag{4.5}$$

Note that we have omitted the radial component $A(\vec{r})$ in the above expression for simplicity. Under the effect of turbulence, the spatial degree of freedom suffers from modal crosstalk which leads to the broadening of the modal spectrum [121, 122]:

$$|\ell\rangle \rightarrow \sum_{\ell'=-\infty}^{+\infty} \alpha_{\ell-\ell'}|\ell'\rangle, \tag{4.6}$$

with $\sum|\alpha_\ell|^2 = 1$. The transformation of the initial vector state is thus expressed as

$$|U\rangle_{\ell}^{in} \rightarrow |U\rangle_{\ell'}^{out} = \sum_{\ell'=-\infty}^{+\infty} \alpha_{\ell-\ell'}|\ell'\rangle|R\rangle + \sum_{\ell'=-\infty}^{+\infty} \beta_{-\ell-\ell'}|\ell'\rangle|L\rangle. \tag{4.7}$$

Considering only vector modes in one particular OAM subspace, $\ell = 1$ in this case, we obtain

$$|U\rangle_{\ell'}^{out} = \alpha_{+2}|-1\rangle|R\rangle + \alpha_0|1\rangle|R\rangle + \beta_0|-1\rangle|L\rangle + \beta_{-2}|1\rangle|L\rangle + \sum(\cdots). \tag{4.8}$$

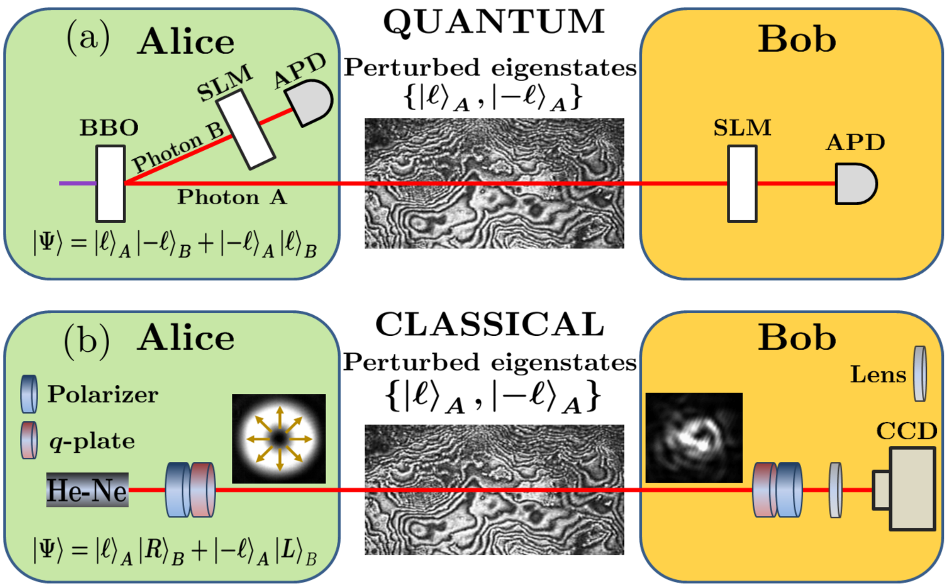

Figure 4.4: Conceptual transport of entangled states through turbulence. (a) Alice generates entangled photon with a non-linear Barium-Borate crystal (BBO), of which she keeps one (Photon B) and sends one (Photon A) to Bob through a free-space turbulent channel. Due to the entanglement of the two photons, The perturbations incurred by photon A will affect the state of Photon B. In a (b) classical equivalent setup, Alice communicates with Bob using a vector vortex beam that she sends through the same turbulent channel. This perturbs the spatial degree of freedom, and though the polarisation degree of freedom is insensitive to turbulence, the classical correlation are affected.

Assuming an identical decay for the degenerate $|\ell\rangle$ and $|-\ell\rangle$ states, that is $\alpha_{+2} = \beta_{-2}$ and $\alpha_0 = \beta_0$, and neglecting higher order terms in $\sum(\cdots)$, we can write

$$|U\rangle_{\ell'}^{out} = \sum_{\ell'=-1,1} \alpha_{1-\ell'}(|\ell'\rangle|R\rangle + |-\ell'\rangle|L\rangle) = \sum_{\ell'=-1,1} \alpha_{1-\ell'}|U\rangle_{\ell'}^{in} \tag{4.9}$$

Using Eq. 4.9, we derive the following transformations for the four vector vector modes of interest:

$$|\mathrm{TE}_{01}\rangle \rightarrow |U\rangle_{\ell'}^{out} = \alpha_{-2}|\mathrm{HE}_{21}^{o}\rangle + \alpha_0|\mathrm{TE}_{01}\rangle, \tag{4.10}$$
$$|\mathrm{TM}_{01}\rangle \rightarrow |U\rangle_{\ell'}^{out} = \alpha_{-2}|\mathrm{HE}_{21}^{e}\rangle + \alpha_0|\mathrm{TM}_{01}\rangle, \tag{4.11}$$
$$|\mathrm{HE}_{21}^{e}\rangle \rightarrow |U\rangle_{-\ell'}^{out} = \alpha_{+2}|\mathrm{TM}_{01}\rangle + \alpha_0|\mathrm{HE}_{21}^{e}\rangle, \tag{4.12}$$
$$|\mathrm{HE}_{21}^{o}\rangle \rightarrow |U\rangle_{-\ell'}^{out} = \alpha_{+2}|\mathrm{TE}_{01}\rangle + \alpha_0|\mathrm{HE}_{21}^{o}\rangle. \tag{4.13}$$

The above transformations describe the different crosstalk channels for a given input state.

In [119] Tyler *et al.* showed that in strong turbulence, all the OAM states are populated with equal probability, resulting in a loss of entanglement as the final superposition is separable with respect to the degrees of freedom

$$|U\rangle_{\ell'}^{out} = \sum_{\ell'=-\infty}^{+\infty} \alpha(|\ell'\rangle|R\rangle + |-\ell'\rangle|L\rangle) = \sum_{\ell'=-\infty}^{+\infty} \alpha|\ell'\rangle(|R\rangle + |L\rangle). \tag{4.14}$$

The decay of entanglement in turbulence can be quantified by considering the evolution of the concurrence as a function of the turbulence strength. Turbulence is defined as the variation in the index of refraction in the air as a result of temperature fluctuations [123]. To measure these variations, we use the Strehl ratio (SR) defined as

$$\mathrm{SR} = \frac{1}{1 + 6.88(\omega_0/r_0)^{5/3}}, \tag{4.15}$$

where

$$r_0 = 0.185(\frac{\lambda^2}{C_n^2 z})^{3/5} \tag{4.16}$$

is Fried's parameter and C_n^2 is the refractive index structure of the turbulent medium, which quantifies the strength of index fluctuations. The propagation distance is z, ω_0 is the width of the fundamental Gaussian beam with wavelength λ. Experimentally, the strehl ratio is measured as the product of the on-axis irradiance of a Gaussian beam in turbulence (I') to that without turbulence (I_0)

$$\mathrm{SR} = I'/I_0. \tag{4.17}$$

such that SR $\in (0, 1]$. When only one of the photon goes through the turbulent channel, as is the case here, the concurrence of an initial maximally entangled states given by Eq. 4.5 is given in terms of the turbulence strength by

$$\mathscr{C}(\mathrm{SR}) = \frac{\mathrm{SR}}{\mathrm{SR}^2 - \mathrm{SR} + 1}. \tag{4.18}$$

In very strong turbulence, SR $\to 0$, the concurrence tends to 0; the final state is therefore separable. Conversely, in the absence of turbulence, SR $\to 1$, the concurrence tends to 1; the final state is non-separable. This evolution of the concurrence agrees with the prediction from the crosstalk model.

We proceeded to verify the above predictions experimentally with the setup shown in Fig. 4.5. A linearly polarised Gaussian beam with radius $\omega_0 = 0.45$ mm was modulated with a half-wave plate and a q-plate to generate a vector vortex beam that was then passed through a thin screen that simulated atmospheric turbulence based on Kolmogorov's theory [124]. In this theory, the atmosphere is modelled as an incompressible fluid. In the atmosphere, fluctuations in temperature are responsible for the variations refractive index. As temperature and velocity fluctuations follow the same spectral laws, the Kolmogorov power spectrum is thus derived from velocity fluctuations and is given by [123]

$$\Phi_n(\kappa) = 0.033 C_n^2 \kappa^{-11/3}, \text{ with } 1/L_0 \leq \kappa \leq 1/l_0, \tag{4.19}$$

where L_0 and l_0 are the inner and outer scales of the turbulence and define the limits within which the above power spectrum describes an isotropic and homogeneous atmosphere. The turbulence phase screen are generated by Fourier transforming the product of a random function with the power spectrum above. This was done digitally and encoded on a SLM and the perturbed vector beam was analysed by a vector mode detector to evaluate the inter-modal crosstalk and a tomography detector to compute the concurrence.

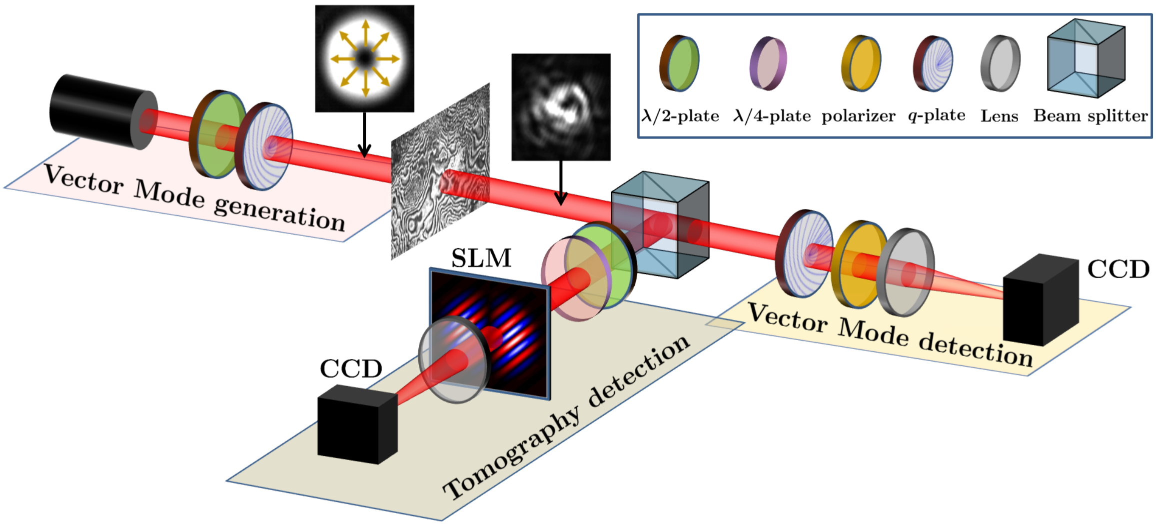

Figure 4.5: Experimental transport of vector vortex beams through atmospheric turbulence. A linearly polarised Gaussian was transformed into a vector vortex beams using half-wave plate and a q-plate and passed through a thin turbulence screen. The perturbed state was then analysed by two detection schemes: a tomography detector to compute the concurrence and a vector mode detector to measure the inter-modal crosstalk by modal decomposition.

The results from Fig 4.6 show the broadening of the OAM spectrum with increasing turbulence, measured for an input $|\mathrm{TM}_{01}\rangle$ mode. We noted that the broadening was not symmetric for $\ell = \pm 1$ as shown in [119, 120]. Consequently, the coupling among the vector modes was observed to be stochastic with increasing turbulence as shown in Fig.4.7, unlike what we predicted above.

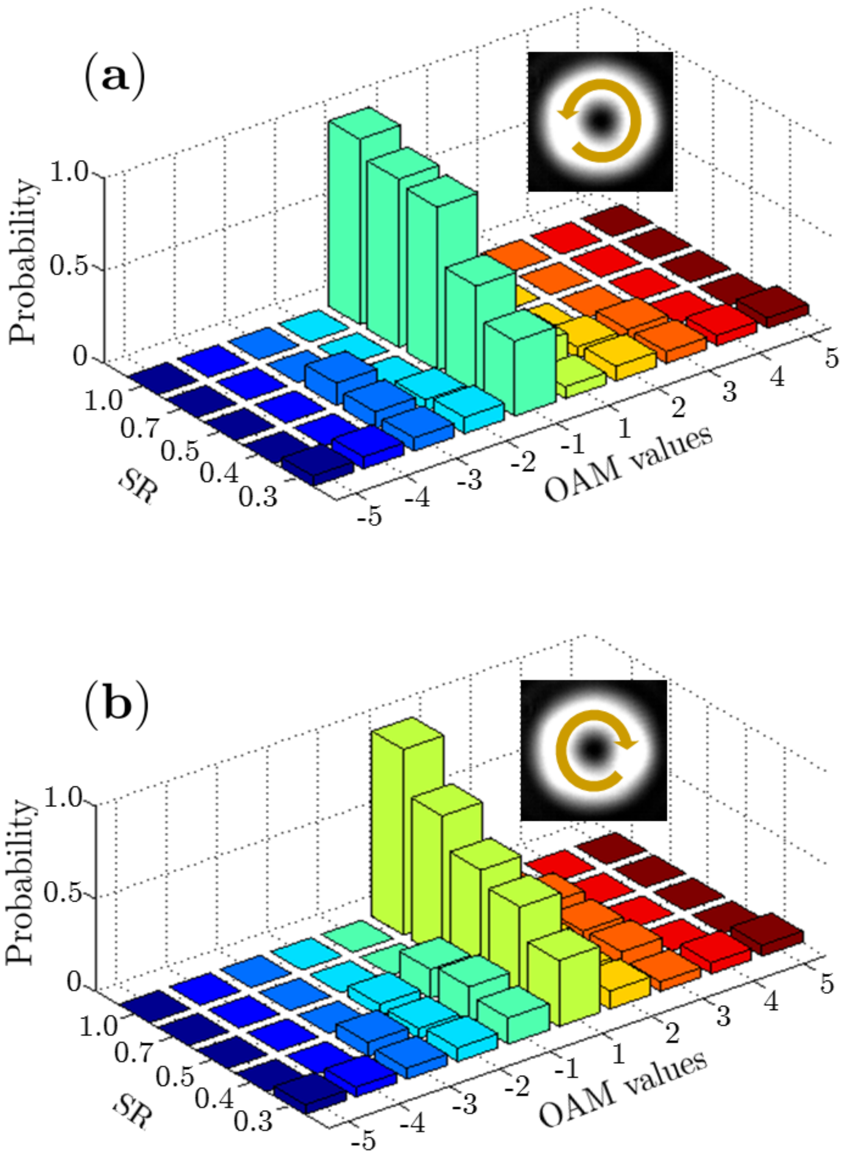

Figure 4.6: Experimental crosstalk determined for an input $|\text{TM}_{01}\rangle$ mode. (a) shows the decay of the $\ell = 1$ state and (b) that of the $\ell = 1$

.

Nonetheless, the modal coupling observed among OAM eigenstates and the four vector modes supported the idea entanglement was lost with increasing turbulence. However, we argued that the classical and quantum setups described in Fig. 4.4 were equivalent. This requires the dynamics of the quantum and classical entanglement to be matched. To this end, we measured the evolution of the entanglement in both the classical and quantum cases. For the quantum experiment a 3 mm BBO crystal was pumped with a picosecond laser operating at 355 nm to produce non-collinear

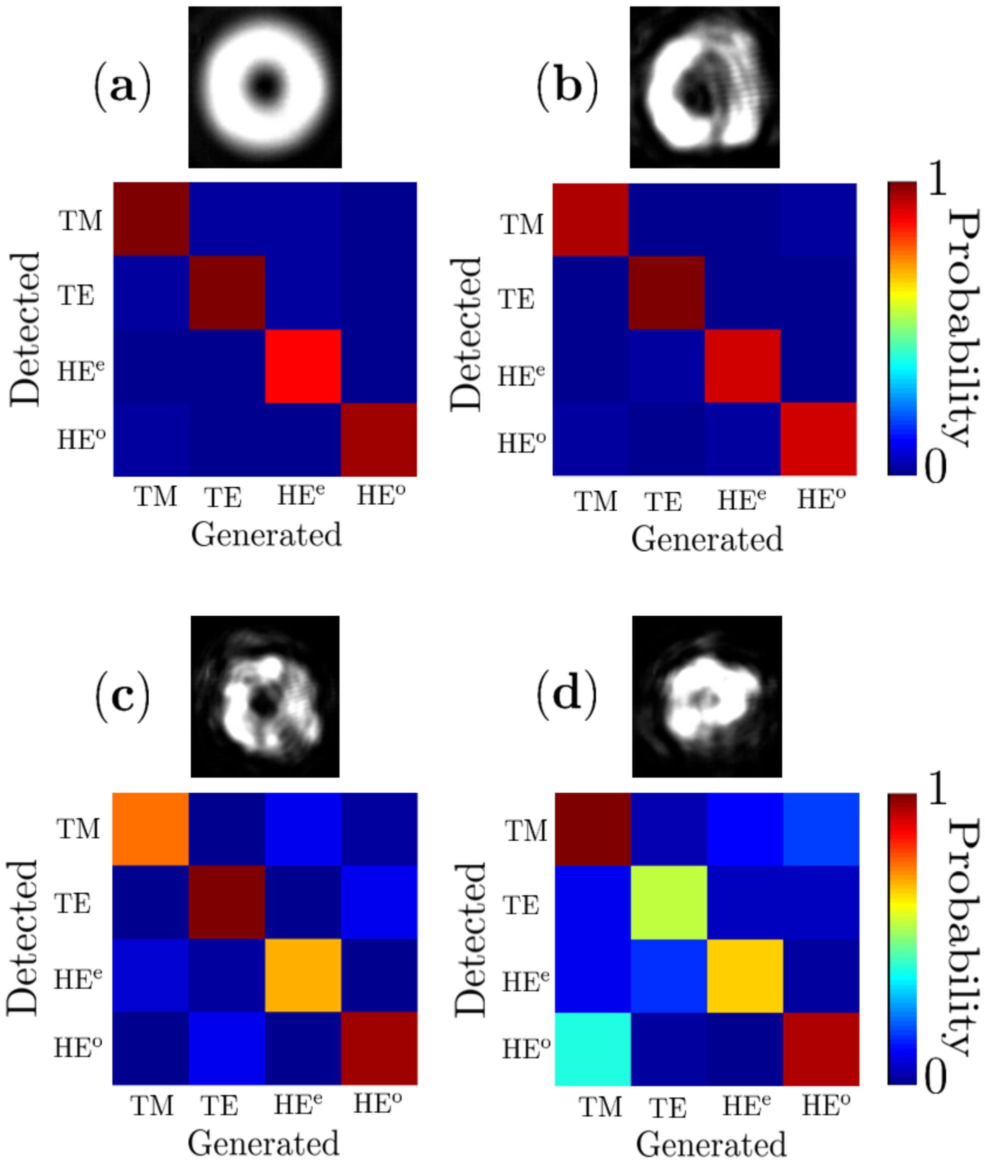

Figure 4.7: Experimental crosstalk of vector vortex modes measured for turbulence strengths of (a) SR =1, (b) SR = 0.7, (c) SR = 0.5 and (d) SR = 0.2

entangled photons by spontaneous parametric down conversion. The two photons were directed on two SLMs where entanglement was measured in the OAM basis, with one of the SLMs having the turbulence screens imposed on the OAM hologram. Both SLM outputs were then coupled to single mode fibres and directed onto avalanche photodiodes connected to a coincidence counter.

The mode size in the quantum experiment was 0.36 mm, differing from the 0.45 mm used for the classical experiment. The concurrence is dependent, through the

Strehl ratio, upon the mode size ω_0. Substituting Eq. 4.15 into Eq. 4.18, we plotted the concurrence as a function of Fried's parameter for the two mode sizes. The differing sizes thus required the results to be normalized. In this case, we normalized the quantum results with respect to the classical ones. We defined the ratio between the classical and quantum theories (CQR) as

$$\mathrm{CQR}(r_0) = \frac{\mathscr{C}(r_0, \omega_{cl})}{\mathscr{C}(r_0, \omega_{qm})}, \tag{4.20}$$

where ω_{cl} and ω_{qm} are the mode sizes used in the classical and quantum experiments respectively. The quantum results were then normalized as follow

$$\mathscr{C}_{norm}(\mathrm{SR}) = \mathscr{C}_{exp}(\mathrm{SR}) \times \mathrm{CQR}(\mathrm{SR}) \tag{4.21}$$

where $\mathscr{C}_{exp}(\mathrm{SR})$ and $\mathscr{C}_{norm}(\mathrm{SR})$ are the experimental and normalized concurrences. The conversion from r_0 to SR is achieved by inverting Eq. 4.15.

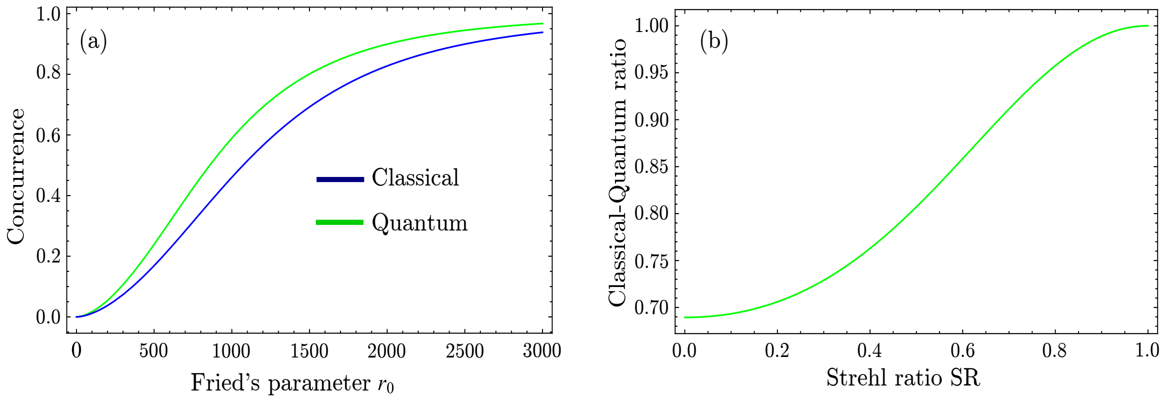

Figure 4.8: Normalization of the quantum and classical theoretical results. (a) shows the variation of the concurrence with turbulence expressed in terms of the Fried's parameter for the mode sizes used in the classical and quantum experiment. (b) shows the theoretical ratio of the classical to the quantum models as a function of the turbulence expressed in terms of the Strehl ratio.

The normalized results in Fig. 4.9 show that the classical systems does indeed model the quantum experiment. With increasing turbulence, the classical and quantum states both decohere and the entanglement decays.

4.4 Conclusion

We have shown in this Chapter that classical non-separable states can be used to model quantum entangled systems. We modelled the evolution of entanglement in

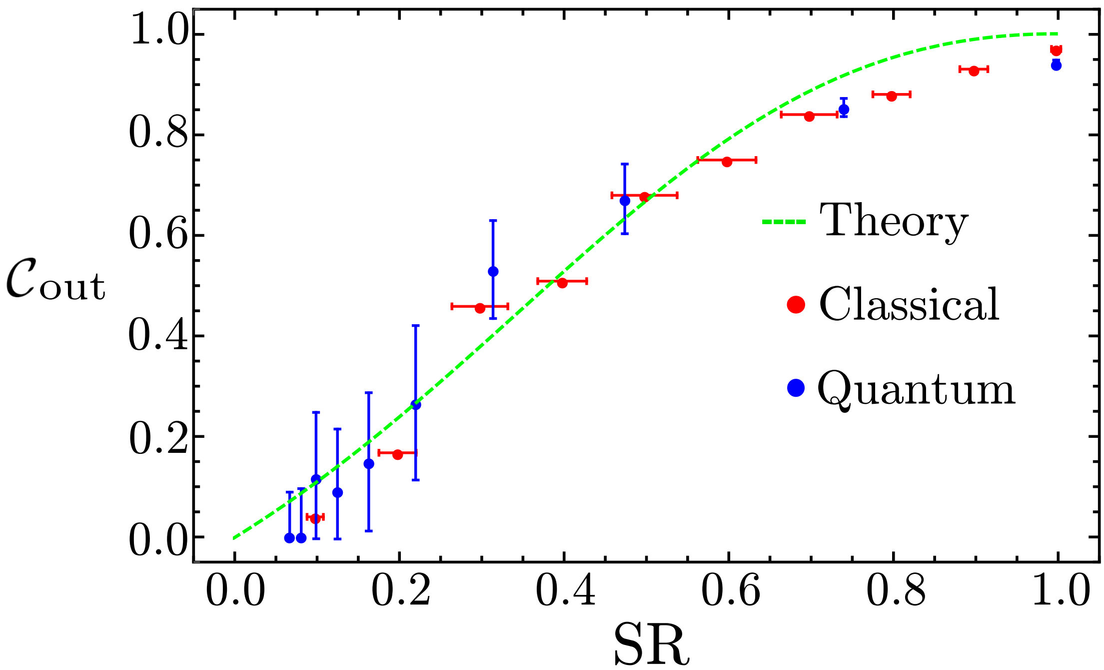

Figure 4.9: Experimental variation of the entanglement with respect to the turbulence strength. the classical results were obtained for an input $|\mathrm{TM}_{01}\rangle$ mode perturbed by phase screens modelling various turbulence strengths SR. After performing a state tomography on each of the various outputs, the concurrence was computed. The quantum results were obtained by perturbing one of two entangled photons with the same phase screens. The green dashed line represents the theoretical curve.

communication media with vector vortex modes propagated through two noisy channels: an optical fibre and a turbulent free-space channel. To measure the degree of non-separability, we used the concurrence, a measure of entanglement in quantum mechanics. We showed, in fibres, that entanglement is preserved after a few centimetres of propagation. We also showed that as a result of fibre imperfections, energy can be exchanged between among the modes, affecting entanglement correlations. In turbulence, we showed, based on two equivalent systems, one quantum and the other classical, that the predictions and results from both systems are identical: the evolution of entanglement as predicted and measured for a quantum entangled system agrees with the classical one. In fibres and free-space, our results show that classical bright sources can be used to characterise quantum links that use entanglement as a resource.

Chapter 5

Conclusions

The focus of the work detailed in this dissertation was to explore the potential of spatial modes of light for optical communication, classical and quantum. We were particularly interested in spatial modes carrying orbital angular momentum (OAM); they offer the possibility of transmitting an infinite amount of information through the additional OAM channels.

In Chapter 2, we demonstrated theoretically and experimentally, that by manipulating the dynamic and geometric phase of light, digitally or statically, we can generate and detect spatial modes of two types: scalar modes and vector modes. We made the distinction between the two type in terms of the separability of their degrees of freedom: scalar modes have separable spatial and polarisation degrees of freedom while vector modes do not. We applied these techniques to the study of classical and quantum communication.

For classical communication, we have shown, using scalar modes and digital holograms, that optical fields carrying OAM could be tailored and multiplexed to increase the communication bandwidth in both free-space and optical fibres. We characterized both optical media to determine the amount of modal coupling they introduced, and used the channels to transmit images. In the process we implemented various encoding techniques based on single mode transmission and mode multiplexing. Using Laguerre-Gaussian modes, we have demonstrated a channels with 100 spatial channels having the potential of increasing the bandwidth of current systems by two orders of magnitudes.

For quantum communication, we have shown that, using vector vortex modes, quantum systems can be modelled using bright sources. For information sharing in quantum links, optical fibres and free-space are two of the available media, each presenting their own challenges: imperfections and birefringence in fibres and turbulence in free-space are two of the most notable ones. Taking advantage of the non-separability of vector modes, and their similarities with quantum entangled systems, we modelled evolution of entanglement in both media: in fibres, we show that entanglement is preserved over a few centimetres, in agreement with past research. However, the perturbation caused by fibres affects both non-separable degrees of freedom of vector beam, making the modelling of the channel non trivial. In turbulent free-space however, the polarisation is unaffected by turbulence. We used this property to model the transport of entangled states through a turbulent link, and showed that both classical and theory are in agreement.

There are however limitations to how much the quantum world can be emulated classically. A quantum process vital to communication is secret key distribution, whereby messages are encrypted with a highly secure key that is exchanged by two parties with single photons. The security of quantum key distribution is linked to the dimensionality of the degrees of freedom available for encoding. Unlike classical systems such as vector vortex beams, quantum states offer the possibility of entanglement in dimensions higher than two. In future research, we aim to shape single photons, to realise high dimensional entanglement transport, in both free-space and fibres, and apply it to increase the dimensionality, and therefore the security, of current quantum key distribution protocols.

Bibliography

[1] D. M. Spirit and P. E. Barnsley, "Optical Time Division Multiplexing: Systems and Networks," *IEEE Communications Magazine*, pp. 56–62, 1994.

[2] M. I. Hayee, M. C. Cardakli, a. B. Sahin, and a. E. Willner, "Doubling of bandwidth utilization using two orthogonal polarizations and power unbalancing in a polarization-division-multiplexing scheme," *IEEE Photonics Technology Letters*, vol. 13, no. 8, pp. 881–883, 2001.

[3] A. Banerjee, Y. Park, F. Clarke, H. Song, S. Yang, G. Kramer, K. Kim, and B. Mukherjee, "Wavelength-division-multiplexed passive optical network (WDM-PON) technologies for broadband access: a review [Invited]," *Journal of Optical Networking*, vol. 4, no. 11, p. 737, 2005.

[4] G. P. Agrawal, *Fiber-Optic Communication Systems*, Wiley-Interscience, 3rd Ed., New York, USA, 2002.

[5] P. E. Green, "Fiber to the home: The next big broadband thing," *IEEE Communications Magazine*, vol. 42, no. 9, pp. 100–106, 2004.

[6] T. Koonen, "Fiber to the Home/Fiber to the Premises: What, Where, and When?," *Proceedings of the IEEE*, vol. 94, no. 5, pp. 911–934, 2006.

[7] H. Willebrand and B. Ghuman, "Fiber optics without fiber," *IEEE Spectrum*, vol. 38, no. 8, pp. 40–45, 2001.

[8] E. Desurvire, *Erbium-doped fiber amplifiers: principles and applications*, Wiley-Interscience, New York, USA, 2002.

[9] C. Berrou, A. Glavieux, and P. Thitimajshima, "Near Shannon Limit Error - Correcting Coding and Decoding : Turbo-Codes (1)," *Communications, 1993. ICC '93 Geneva. Technical Program, Conference Record, IEEE International Conference*, no. 1, pp. 1064 – 1070 vol.2, 1993.

[10] D. J. Richardson, J. M. Fini, and L. E. Nelson, "Space-division multiplexing in optical fibres," *Nature Photonics*, vol. 7, no. 5, pp. 354–362, 2013.

[11] a.D. Ellis, J. Z. J. Zhao, and D. Cotter, "Approaching the Non-Linear Shannon Limit," *Journal of Lightwave Technology*, vol. 28, no. 4, pp. 423–433, 2010.

[12] L. Allen, M. W. Beijersbergen, R. J. C. Spreeuw, and J. P. Woerdman, "Orbital angular momentum of light and the transformation of Laguerre-Gaussian laser modes," *Physical Review A*, vol. 45, no. 11, pp. 8185–8189, 1992.

[13] G. Gibson, J. Courtial, M. Padgett, M. Vasnetsov, V. Pas'ko, S. Barnett, and S. Franke-Arnold, "Free-space information transfer using light beams carrying orbital angular momentum.," *Optics Express*, vol. 12, no. 22, pp. 5448–5456, 2004.

[14] J. Wang, J.-Y. Yang, I. M. Fazal, N. Ahmed, Y. Yan, H. Huang, Y. Ren, Y. Yue, S. Dolinar, M. Tur, and A. E. Willner, "Terabit free-space data transmission employing orbital angular momentum multiplexing," *Nature Photonics*, vol. 6, no. 7, pp. 488–496, 2012.

[15] N. Bozinovic, Y. Yue, Y. Ren, M. Tur, P. Kristensen, H. Huang, A. E. Willner, and S. Ramachandran, "Terabit-Scale Orbital Angular Momentum Mode Division Multiplexing in Fibers," *Science*, vol. 340, pp. 1545–1548, 2013.

[16] B.-J. Pors, F. Miatto, G. W. t Hooft, E. R. Eliel, and J. P. Woerdman, "High-dimensional entanglement with orbital-angular-momentum states of light," *Journal of Optics*, vol. 13, 064008, 2011.

[17] a.C. Dada, J. Leach, G. Buller, M. Padgett, and E. Andersson, "Experimental high-dimensional two-photon entanglement and violations of generalized Bell inequalities," *Nature Physics*, vol. 7, no. 9, pp. 677–680, 2011.

[18] J. Romero, D. Giovannini, S. Franke-Arnold, S. M. Barnett, and M. J. Padgett, "Increasing the dimension in high-dimensional two-photon orbital angular momentum entanglement," *Physical Review A*, vol. 86, 012334, 2012.

[19] V. Scarani, H. Bechmann-Pasquinucci, N. J. Cerf, M. Dušek, N. Lütkenhaus, and M. Peev, "The security of practical quantum key distribution," *Reviews of Modern Physics*, vol. 81, no. 3, pp. 1301–1350, 2009.

[20] J. H. Poynting, "The Wave Motion of a Revolving Shaft, and a Suggestion as to the Angular Momentum in a Beam of Circularly Polarised Light," *Proceedings of the Royal Society A: Mathematical, Physical and Engineering Sciences*, vol. 82, no. 557, pp. 560–567, 1909.

[21] R. A. Beth, "Mechanical detection and measurement of the angular momentum of light," *Physical Review*, vol. 50, pp. 115–125, 1936.

[22] A. M. Yao and M. J. Padgett, "Orbital angular momentum: origins, behavior and applications," *Advances in Optics and Photonics*, vol. 3, p. 161, 2011.

[23] B. Jack, a. M. Yao, J. Leach, J. Romero, S. Franke-Arnold, D. G. Ireland, S. M. Barnett, and M. J. Padgett, "Entanglement of arbitrary superpositions of modes within two-dimensional orbital angular momentum state spaces," *Physical Review A*, vol. 81, no. 4, 043844, 2010.

[24] A. Einstein, B. Podolsky, and N. Rosen, "Can Quantum-Mechanical Description of Physical Reality Be Considered Complete?," *Physical Review*, vol. 47, pp. 777–780, 1935.

[25] J. Preskill, "Quantum Information and Computation. Lecture Notes.," *Physics Today*, pp. 24–30, 1998.

[26] D. Bouwmeester, J.-W. Pan, K. Mattle, M. Eibl, H. Weinfurter, and A. Zeilinger, "Experimental quantum teleportation," *Nature*, vol. 390, no. 6660, pp. 575–579, 1997.

[27] A. K. Ekert, "Quantum Cryptography Based on Bell's Theorem," *Physical Review Letters*, vol. 67, no. 6, pp. 661–663, 1991.

[28] J. T. Barreiro, N. K. Langford, N. a. Peters, and P. G. Kwiat, "Generation of hyperentangled photon pairs," *Physical Review Letters*, vol. 95, no. 26, pp. 1–4, 2005.

[29] A. W. Snyder and J. D. Love, *Optical Waveguide Theory*, vol. 2, Springer, Boston, USA, 1984.

[30] R. Ferraro, *Einstein's Space-Time: An Introduction to Special and General Relativity*, Springer, New York, USA, 2007.

[31] J. S. Bell, "On the Einstein Podolsky Rosen paradox," *Physics*, vol. 1, no. 3, pp. 195–200, 1964.

[32] G. Weihs, T. Jennewein, C. Simon, H. Weinfurter, and A. Zeilinger, "P Hysical R Eview Letters," *Physical Review Letters*, vol. 82, pp. 1–5, 1998.

[33] M. McLaren, T. Konrad, and A. Forbes, "Measuring the nonseparability of vector vortex beams," *Physical Review A*, vol. 92, no. 2, p. 023833, 2015.

[34] C. V. S. Borges, M. Hor-Meyll, J. A. O. Huguenin, and A. Z. Khoury, "Bell-like inequality for the spin-orbit separability of a laser beam," *Physical Review A*, vol. 82, no. 3, p. 033833, 2010.

[35] G. Milione, H. I. Sztul, D. a. Nolan, and R. R. Alfano, "Higher-order poincaré sphere, stokes parameters, and the angular momentum of light," *Physical Review Letters*, vol. 107, no. 5, pp. 1–4, 2011.

[36] R. J. C. Spreeuw, "Classical wave-optics analogy of quantum-information processing," *Physical Review A*, vol. 63, no. 6, p. 062302, 2001.

[37] A. Aiello, F. Töppel, C. Marquardt, E. Giacobino, and G. Leuchs, "Classical entanglement: Oxymoron or resource?," e-print, arXiv:1409.0213 [quant-ph], pp. 1–9, 2014.

[38] P. Ghose and A. Mukherjee, "Entanglement in Classical Optics," *Reviews in Theoretical Science*, vol. 2, pp. 274–288, 2014.

[39] G. Turnbull, D. Robertson, G. Smith, L. Allen, and M. Padgett, "Generation of free-space Laguerre-Gaussian modes at millimetre-wave frequencies by use of a spiral phaseplate," *Optics Communications*, vol. 127, pp. 183–188, 1996.

[40] M. Beijersbergen, R. Coerwinkel, M. Kristensen, and J. Woerdman, "Helical-wavefront laser beams produced with a spiral phaseplate," *Optics Communications*, vol. 112, pp. 321–327, 1994.

[41] S. S. R. Oemrawsingh, J. A. W. van Houwelingen, E. R. Eliel, J. P. Woerdman, E. J. K. Verstegen, J. G. Kloosterboer, and G. W. t. Hooft, "Production and characterization of spiral phase plates for optical wavelengths," *Applied Optics*, vol. 43, pp. 688–694, 2004.

[42] V. Lakshminarayanan, M. L. Calvo, and T. Alieva, *Mathematical Optics: Classical, Quantum, and Computational Methods.* CRC Press, Florida, USA, 2012.

[43] D. G. Grier, "A revolution in optical manipulation.," *Nature*, vol. 424, no. 6950, pp. 810–816, 2003.

[44] J. R. Moffitt, Y. R. Chemla, S. B. Smith, and C. Bustamante, "Recent advances in optical tweezers.," *Annual review of biochemistry*, vol. 77, pp. 205–228, 2008.

[45] A. M. Weiner, A. M. Weiner, I. Since, and I. Since, "Femtosecond pulse shaping using spatial light modulators," *Review of Scientific Instruments*, vol. 71, pp. 1929–1960, 2000.

[46] R. Fiolka, M. Beck, and A. Stemmer, "Structured illumination in total internal reflection fluorescence microscopy using a spatial light modulator," *Optics Letters*, vol. 33, pp. 1629–1631, 2008.

[47] P. Kner, B. B. Chhun, E. R. Griffis, L. Winoto, and M. G. L. Gustafsson, "Super-resolution video microscopy of live cells by structured illumination," *Nature Methods*, vol. 6, no. 5, pp. 339–42, 2009.

[48] B. Huang, H. Babcock, and X. Zhuang, "Breaking the Diffraction Barrier: Super-Resolution Imaging of Cells," *Cell*, vol. 143, no. 7, pp. 1047–1058, 2010.

[49] V. Arrizón, U. Ruiz, R. Carrada, and L. a. González, "Pixelated phase computer holograms for the accurate encoding of scalar complex fields.," *Journal of the Optical Society of America. A, Optics, image science, and vision*, vol. 24, pp. 3500–3507, 2007.

[50] I. a. Litvin, A. Dudley, F. S. Roux, and A. Forbes, "Azimuthal decomposition with digital holograms," *Optics Express*, vol. 20, no. 10, p. 10996, 2012.

[51] D. Flamm, D. Naidoo, C. Schulze, A. Forbes, and M. Duparré, "Mode analysis with a spatial light modulator as a correlation filter," *Optics Letters*, vol. 37, pp. 2478–2480, 2012.

[52] C. Schulze, A. Dudley, D. Flamm, M. Duparré, and A. Forbes, "Measurement of the orbital angular momentum density of light by modal decomposition," *New Journal of Physics*, vol. 15, no.7, pp. 1023–1032, 2013.

[53] Q. Zhan, "Cylindrical vector beams: from mathematical concepts to applications," *Advances in Optics and Photonics*, vol. 1, p. 1, 2009.

[54] K. Yonezawa, Y. Kozawa, and S. Sato, "Generation of a radially polarized laser beam by use of the birefringence of a c-cut Nd:YVO4 crystal," *Optics Letters*, vol. 31, p. 2151, 2006.

[55] J.-F. Bisson, J. Li, K. Ueda, and Y. Senatsky, "Radially polarized ring and arc beams of a neodymium laser with an intra-cavity axicon," *Optics Express*, vol. 14, p. 3304, 2006.

[56] Q. Zhan and J. R. Leger, "Interferometric measurement of the geometric phase in space-variant polarization manipulations," *Optics Communications*, vol. 213, pp. 241–245, 2002.

[57] G. Machavariani, Y. Lumer, I. Moshe, A. Meir, and S. Jackel, "Spatially-variable retardation plate for efficient generation of radially- and azimuthally-polarized beams," *Optics Communications*, vol. 281, pp. 732–738, 2008.

[58] M. R. Beversluis, L. Novotny, and S. J. Stranick, "Programmable vector point-spread function engineering," *Optics Express*, vol. 14, p. 2650, 2006.

[59] R. Zheng, C. Gu, A. Wang, L. Xu, and H. Ming, "An all-fiber laser generating cylindrical vector beam.," *Optics Express*, vol. 18, no. 10, pp. 10834–10838, 2010.

[60] L. Marrucci, E. Karimi, S. Slussarenko, B. Piccirillo, E. Santamato, E. Nagali, and F. Sciarrino, "Spin-to-orbital conversion of the angular momentum of light and its classical and quantum applications," *Journal of Optics*, vol. 13, no. 6, 064001, 2011.

[61] M. Young, *Optics and Lasers: Including Fibers and Optical Waveguides*. Springer Berlin Heidelberg, 2013.

[62] J. Kim, Y. Li, M. N. Miskiewicz, C. Oh, M. W. Kudenov, and M. J. Escuti, "Fabrication of ideal geometric-phase holograms with arbitrary wavefronts," *Optica*, vol. 2, no. 11, p. 958, 2015.

[63] M. V. Berry, "Quantal Phase Factors Accompanying Adiabatic Changes," *Proceedings of the Royal Society of London A: Mathematical, Physical and Engineering Sciences*, vol. 392, no. 1802, pp. 45–57, 1984.

[64] S. Pancharatnam, "Generalized theory of interference and its applications - Part I. Partially coherent pencils," *Proceedings of the Indian Academy of Sciences - Section A*, vol. 44, pp. 398–417 1956.

[65] E. J. S. Jorge V. Jos, *Classical dynamics. A contemporary approach.* Cambridge University Press, Cambridge, UK, 1998.

[66] G. Jaeger, *Quantum Information: An Overview.* Springer, New York, USA, 2007.

[67] S. Hill and W. K. Wootters, "Entanglement of a Pair of Quantum Bits," *Physical Review Letters*, vol. 78, no. 26, pp. 5022–5025, 1997.

[68] W. K. Wootters, "Entanglement of Formation of an Arbitrary State of Two Qubits," *Physical Review Letters*, vol. 80, no. 10, pp. 2245–2248, 1998.

[69] J. Altepeter, E. Jeffrey, and P. Kwiat, "Photonic State Tomography," in *Advances in Atomic, Molecular and Optical Physics*, vol. 52, pp. 105–159, 2005.

[70] D. F. V. James, P. G. Kwiat, W. J. Munro, and A. G. White, "Measurement of qubits," *Physical Review A*, vol. 64, p. 052312, 2001.

[71] W. K. Wootters and B. D. Fields, "Optimal state-determination by mutually unbiased measurements," *Annals of Physics*, vol. 191, pp. 363–381, 1989.

[72] M. Mafu, A. Dudley, S. Goyal, D. Giovannini, M. McLaren, M. J. Padgett, T. Konrad, F. Petruccione, N. Lütkenhaus, and A. Forbes, "Higher-dimensional orbital-angular-momentum-based quantum key distribution with mutually unbiased bases," *Physical Review A*, vol. 88, no. 3, pp. 1–8, 2013.

[73] A. E. Willner, H. Huang, Y. Yan, Y. Ren, N. Ahmed, G. Xie, C. Bao, L. Li, Y. Cao, Z. Zhao, and Others, "Optical communications using orbital angular momentum beams," *Advances in Optics and Photonics*, vol. 7, no. 1, pp. 66–106, 2015.

[74] I. B. Djordjevic, "Deep-space and near-Earth optical communications by coded orbital angular momentum (OAM) modulation," *Optics Express*, vol. 19, no. 15, p. 14277, 2011.

[75] A. Mair, A. Vaziri, G. Weihs, and A. Zeilinger, "Entanglement of the orbital angular momentum states of photons," *Nature*, vol. 412, no. 6844, pp. 313–316, 2001.

[76] G. Molina-Terriza, J. P. Torres, and L. Torner, "Twisted photons," *Nature Physics*, vol. 3, no. 5, pp. 305–310, 2007.

[77] R. Vasilyeu, A. Dudley, N. Khilo, and A. Forbes, "Generating superpositions of higher-order Bessel beams," *Optics express*, vol. 17, no. 26, pp. 23389–23395, 2009.

[78] C. Schulze, S. Ngcobo, M. Duparré, and A. Forbes, "Modal decomposition without a priori scale information.," *Optics express*, vol. 20, no. 25, pp. 27866–73, 2012.

[79] K. Sasaki, N. Minato, T. Ushikubo, and Y. Arimoto, "First OCDMA Experimental Demonstration over Free Space and Optical Fiber Link," in *Optical Fiber Communication Conference/National Fiber Optic Engineers Conference*, p. OMR8, Optical Society of America, 2008.

[80] R. M. Sova, J. E. Sluz, D. W. Young, J. C. Juarez, A. Dwivedi, N. M. Demidovich III, J. E. Graves, M. Northcott, J. Douglass, J. Phillips, D. Driver, A. McClarin, and D. Abelson, "80 Gb/s free-space optical communication demonstration between an aerostat and a ground terminal," *Proceedings of the SPIE*, vol. 6304, p. 630414, 2006.

[81] Y. B. Band, *Light and Matter: Electromagnetism, Optics, Spectroscopy and Lasers*, John Wiley & Sons, Ltd, West Sussex, UK, 2006.

[82] R. Brüning, Y. Zhang, M. McLaren, M. Duparré, and A. Forbes, "Overlap relation between free-space Laguerre Gaussian modes and step-index fiber modes," *Journal of the Optical Society of America A*, vol. 32, no. 9, p. 1678, 2015.

[83] A. B. Fallahkhair, K. S. Li, and T. E. Murphy, "Vector finite difference modesolver for anisotropic dielectric waveguides," *Journal of Lightwave Technology*, vol. 26, pp. 1423–1431, 2008.

[84] J. Carpenter, B. C. Thomsen, and T. D. Wilkinson, "Degenerate mode-group division multiplexing," *Journal of Lightwave Technology*, vol. 30, no. 24, pp. 3946–3952, 2012.

[85] J. Carpenter, B. J. Eggleton, and J. Schröder, "110X110 Optical Mode Transfer Matrix Inversion," *Optics Express*, vol. 22, no. 1, p. 96, 2014.

[86] P. Martelli, a. Gatto, P. Boffi, and M. Martinelli, "Free-space optical transmission with orbital angular momentum division multiplexing," *Electronics Letters*, vol. 47, no. 17, p. 972, 2011.

[87] H. Huang, G. Xie, Y. Yan, N. Ahmed, Y. Ren, Y. Yue, D. Rogawski, M. J. Willner, B. I. Erkmen, K. M. Birnbaum, S. J. Dolinar, M. P. J. Lavery, M. J. Padgett, M. Tur, and A. E. Willner, "100 Tbit/s free-space data link enabled by three-dimensional multiplexing of orbital angular momentum, polarization, and wavelength," *Optics Letters*, vol. 39, p. 197, 2014.

[88] F. Tamburini and E. Mari and A. Sponselli and B. Thidé and A. Bianchini and F. Romanato, "Encoding many channels on the same frequency through radio vorticity: first experimental test," *New Journal of Physics*, vol. 14, no. 3, p. 033001, 2012.

[89] R. Ryf, M. A. Mestre, S. Randel, S. Member, C. Schmidt, A. H. Gnauck, R.-J. Essiambre, P. J. Winzer, R. Delbue, P. Pupalaikis, A. Sureka, Y. Sun, X. Jiang, D. W. Peckham, A. H. McCurdy, and R. Lingle, "Mode-Multiplexed Transmission Over a 209-km DGD-Compensated Hybrid Few-Mode Fiber Span," *IEEE Photonics Technology Letters*, vol. 24, no. 21, pp. 1965–1968, 2012.

[90] V. Sleiffer, Y. Jung, V. Veljanovski, R. van Uden, M. Kuschnerov, H. Chen, B. Inan, L. G. Nielsen, Y. Sun, D. Richardson, S. Alam, F. Poletti, J. Sahu, A. Dhar, A. Koonen, B. Corbett, R. Winfield, A. Ellis, and H. de Waardt, "737 Tb/s (96 x 3 x 256-Gb/s) mode-division-multiplexed DP-16QAM transmission with inline MM-EDFA," *Optics Express*, vol. 20, p. B428, 2012.

[91] Y. Chen, A. Lobato, Y. Jung, H. Chen, V. A. J. M. Sleiffer, M. Kuschnerov, N. K. Fontaine, R. Ryf, D. J. Richardson, B. Lankl, and N. Hanik, "41.6 Tbit/s C-Band SDM OFDM Transmission Through 12 Spatial and Polarization Modes Over 74.17 km Few Mode Fiber," *Journal of Lightwave Technology*, vol. 33, pp. 1440–1444, 2015.

[92] G. Xie, L. Li, Y. Ren, H. Huang, Y. Yan, N. Ahmed, Z. Zhao, M. P. J. Lavery, N. Ashrafi, S. Ashrafi, R. Bock, M. Tur, A. F. Molisch, and A. E. Willner, "Performance metrics and design considerations for a free-space optical orbital-angular-momentum multiplexed communication link," *Optica*, vol. 2, no. 4, pp. 357–365, 2015.

[93] Y. Ren, G. Xie, H. Huang, C. Bao, Y. Yan, N. Ahmed, M. P. J. Lavery, B. I. Erkmen, S. Dolinar, M. Tur, M. a. Neifeld, M. J. Padgett, R. W. Boyd, J. H. Shapiro, and A. E. Willner, "Adaptive optics compensation of multiple orbital angular momentum beams propagating through emulated atmospheric turbulence.," *Optics letters*, vol. 39, no. 10, pp. 2845–8, 2014.

[94] D.-M. Spangenberg, A. Dudley, P. H. Neethling, E. G. Rohwer, and A. Forbes, "White light wavefront control with a spatial light modulator," *Optics Express*, vol. 22, no. 11, p. 13870, 2014.

[95] G. Milione, M. P. J. Lavery, H. Huang, Y. Ren, G. Xie, T. A. Nguyen, E. Karimi, L. Marrucci, D. A. Nolan, R. R. Alfano, and A. E. Willner, "4 20 Gbit/s mode division multiplexing over free space using vector modes and a q-plate mode (de)multiplexer.," *Optics letters*, vol. 40, pp. 1980–3, 2015.

[96] G. Milione, T. A. Nguyen, J. Leach, D. A. Nolan, and R. R. Alfano, "Using the nonseparability of vector beams to encode information for optical communication," *Optics Letters*, vol. 40, no. 21, p. 4887, 2015.

[97] C. H. Bennett and G. Brassard, "Quantum Cryptography: Public key distribution and coin tossing," *Proceedings of the IEEE International Conference on Computers, Systems, and Signal Processing, Bangalore*, pp. 175–179, 1984.

[98] R. Ursin, F. Tiefenbacher, T. Schmitt-Manderbach, H. Weier, T. Scheidl, M. Lindenthal, B. Blauensteiner, T. Jennewein, J. Perdigues, P. Trojek, B. Ömer, M. Fürst, M. Meyenburg, J. Rarity, Z. Sodnik, C. Barbieri, H. Weinfurter, and A. Zeilinger, "Entanglement-based quantum communication over 144 km," *Nature Physics*, vol. 3, pp. 481–486, 2007.

[99] X.-S. Ma, T. Herbst, T. Scheidl, D. Wang, S. Kropatschek, W. Naylor, B. Wittmann, A. Mech, J. Kofler, E. Anisimova, V. Makarov, T. Jennewein, R. Ursin, and A. Zeilinger, "Quantum teleportation over 143 kilometres using active feed-forward.," *Nature*, vol. 489, no. 7415, pp. 269–73, 2012.

[100] C. Bennett and S. Wiesner, "Communication via one- and two-particle operators on Einstein-Podolsky-Rosen states," *Physical Review Letters*, vol. 69, no. 20, pp. 2881–2884, 1992.

[101] K. Mattle, H. Weinfurter, P. G. Kwiat, and A. Zeilinger, "Dense Coding in Experimental Quantum Communication," *Physical Review Letters*, vol. 76, no. 25, pp. 4656–4659, 1996.

[102] V. D'Ambrosio, E. Nagali, S. P. Walborn, L. Aolita, S. Slussarenko, L. Marrucci, and F. Sciarrino, "Complete experimental toolbox for alignment-free quantum communication," *Nature Communications*, vol. 3, p. 961, 2012.

[103] G. Vallone, V. DAmbrosio, A. Sponselli, S. Slussarenko, L. Marrucci, F. Sciarrino, and P. Villoresi, "Free-Space Quantum Key Distribution by Rotation-Invariant Twisted Photons," *Physical Review Letters*, vol. 113, no. 6, p. 060503, 2014.

[104] R. Horodecki, P. Horodecki, M. Horodecki, and K. Horodecki, "Quantum entanglement," *Reviews of Modern Physics*, vol. 81, no. 2, p. 865, 2009.

[105] J. Romero, D. Giovannini, M. G. McLaren, E. J. Galvez, A. Forbes, and M. J. Padgett, "Orbital angular momentum correlations with a phase-flipped Gaussian mode pump beam," *Journal of Optics*, vol. 14, no. 8, p. 085401, 2012.

[106] M. McLaren, M. Agnew, J. Leach, F. S. Roux, M. J. Padgett, R. W. Boyd, and A. Forbes, "Entangled Bessel-Gaussian beams," *Optics Express*, vol. 20, p. 23589, 2012.

[107] M. Krenn, R. Fickler, M. Huber, R. Lapkiewicz, W. Plick, S. Ramelow, and A. Zeilinger, "Entangled singularity patterns of photons in Ince-Gauss modes," *Physical Review A*, vol. 87, p. 012326, 2013.

[108] W. Löffler, T. G. Euser, E. R. Eliel, M. Scharrer, P. S. J. Russell, and J. P. Woerdman, "Fiber Transport of Spatially Entangled Photons," *Physical Review Letters*, vol. 106, p. 240505, 2011.

[109] Y. Kang, J. Ko, S. M. Lee, S.-K. Choi, B. Y. Kim, and H. S. Park, "Measurement of the Entanglement between Photonic Spatial Modes in Optical Fibers," *Physical Review Letters*, vol. 109, p. 020502, 2012.

[110] R. J. C. Spreeuw, "A classical analogy of entanglement," *Found. Phys.*, vol. 28, pp. 361–374, 1998.

[111] D. Francisco, C. Iemmi, J. Paz, and S. Ledesma, "Simulating a quantum walk with classical optics," *Physical Review A*, vol. 74, no. 5, p. 052327, 2006.

[112] A. Lucesoli and T. Rozzi, "Image transmission and radiation by truncated linearly polarized multimode fiber," *Appl. Opt.*, vol. 46, pp. 3031–3037, 2007.

[113] C. Gopaul and R. Andrews, "The effect of atmospheric turbulence on entangled orbital angular momentum states," *New Journal of Physics*, vol. 9, no. 4, pp. 1–7, 2007.

[114] M. Malik, M. O'Sullivan, B. Rodenburg, M. Mirhosseini, J. Leach, M. P. J. Lavery, M. J. Padgett, and R. W. Boyd, "Influence of atmospheric turbulence on optical communications using orbital angular momentum for encoding.," *Optics express*, vol. 20, no. 12, pp. 13195–200, 2012.

[115] C. Paterson, "Atmospheric Turbulence and Orbital Angular Momentum of Single Photons for Optical Communication," *Physical Review Letters*, vol. 94, no. 15, p. 153901, 2005.

[116] B. J. Smith and M. G. Raymer, "Two-photon wave mechanics," *Physical Review A*, vol. 74, no. 6, p. 062104, 2006.

[117] F. S. Roux, "Infinitesimal-propagation equation for decoherence of an orbital-angular-momentum-entangled biphoton state in atmospheric turbulence," *Physical Review A*, vol. 83, no. 5, p. 053822, 2011.

[118] Y. R. Shen, *The principles of nonlinear optics*. Wiley-Interscience, New York, USA, 2003.

[119] G. A. Tyler and R. W. Boyd, "Influence of atmospheric turbulence on the propagation of quantum states of light carrying orbital angular momentum," *Optics Letters*, vol. 34, p. 142, 2009.

[120] B. Rodenburg, M. P. J. Lavery, M. Malik, M. N. OSullivan, M. Mirhosseini, D. J. Robertson, M. Padgett, and R. W. Boyd, "Influence of atmospheric turbulence on states of light carrying orbital angular momentum," *Optics Letters*, vol. 37, no. 17, p. 3735, 2012.

[121] J. A. Anguita, M. A. Neifeld, and B. V. Vasic, "Turbulence-induced channel crosstalk in an orbital angular momentum-multiplexed free-space optical link.," *Applied optics*, vol. 47, pp. 2414–2429, 2008.

[122] Y. Ren, H. Huang, G. Xie, N. Ahmed, Y. Yan, B. I. Erkmen, N. Chandrasekaran, M. P. J. Lavery, N. K. Steinhoff, M. Tur, S. Dolinar, M. Neifeld, M. J. Padgett, R. W. Boyd, J. H. Shapiro, and A. E. Willner, "Atmospheric turbulence effects on the performance of a free space optical link employing orbital angular momentum multiplexing," *Optics letters*, vol. 38, no. 20, pp. 4062–5, 2013.

[123] L. C. Andrews and R. L. Phillips, *Laser Beam Propagation through Random Media*, vol. 1. 2nd Ed, SPIE, Washington, USA, 2005.

[124] A. N. Kolmogorov, "The local structure of turbulence in incompressible viscous fluid for very large Reynolds numbers," *Doklady Akademii Nauk Sssr*, vol. 30, no. 1890, pp. 301–305, 1941.